Physics of Fluids

RESEARCH ARTICLE | FEBRUARY 21 2024

Effects of swirling inflow on the stability and combustion mode of rotating detonations ✓

Xinke Shao (邵新科) ; Zijian Zhang (张子健) ✉ ; Lisong Shi (时立松) ; Hanli Huang (黄瀚黎);
Chihyung Wen (温志湧)

Physics of Fluids 36, 026116 (2024)
https://doi.org/10.1063/5.0190314

Physics of Fluids ARTICLE pubs.aip.org/aip/pof

Effects of swirling inflow on the stability and combustion mode of rotating detonations

Cite as: Phys. Fluids **36**, 026116 (2024); doi: 10.1063/5.0190314
Submitted: 5 December 2023 · Accepted: 24 January 2024 ·
Published Online: 21 February 2024

Xinke Shao (邵新科),[1] Zijian Zhang (张子健),[1,a)] Lisong Shi (时立松),[1] Hanli Huang (黄瀚黎),[2]
and Chihyung Wen (温志湧)[1]

AFFILIATIONS

[1]Department of Aeronautical and Aviation Engineering, The Hong Kong Polytechnic University, Hong Kong, China
[2]National Key Laboratory of Transient Physics, Nanjing University of Science and Technology, Nanjing, Jiangsu, China

[a)]Author to whom correspondence should be addressed: zijzhang@polyu.edu.hk

ABSTRACT

In this study, a novel approach for enhancing the stability of rotating detonation waves (RDWs) with the use of a swirling inflow strategy is presented. A series of numerical simulations are carried out by solving the two-dimensional reactive Navier–Stokes equations. The effects of the swirling angle on the stability of the RDWs and the combustion mode are analyzed. The results show that the formation of the burnt gas bumps is suppressed by the implementation of a swirling inflow. The swirling inflow also contributes to an increased homogeneity of the reactant within the fuel refill zone. As a result, a remarkable enhancement of the stability of the RDWs in terms of their oscillations in heights and inclined angles is achieved without an apparent compromise of the heights of the RDWs. The propagation speeds of the RDWs are controllable within a wide range approximately from 81% to 114% of the Chapman–Jouguet detonation speed by adjusting the swirling angle. Moreover, the oscillations in the instantaneous fuel consumption rates of both detonative and deflagrative combustion are dominated by the oscillation in the height of the RDW; hence, the swirling inflow reduces the oscillations in these two fuel consumption rates and subsequently the detonation fraction. Consequently, the smoothness of the performance output in terms of specific impulses can be significantly improved with a reduced standard deviation of oscillation up to 84% by the implementation of swirling inflows, and the averaged specific impulse only encounters a small deficit of no more than 7.4%.

I. INTRODUCTION

A detonation wave (DW) has a strong discontinuity in both pressure and temperature when the burned products are quickly formed behind the DW and do not have time to expand; this results in a nearly constant-volume mode of combustion.[1] Accordingly, detonation-based engines are attracting increasing research interest worldwide due to their high thermodynamic efficiency.[2–7] As a promising detonation-based engine, the rotating detonation engine (RDE) possesses several advantages, such as compact configuration, high operating frequency, and the sustained presence of DWs.[2,6,8] In recent years, increasing numbers of investigations regarding RDEs have been extensively carried out, showing that the RDEs have become the frontier of aerospace propulsion technology.

During the operation of an RDE, the flow field within the combustor always exhibits inherent unsteadiness, characterized by the presence of multiple instabilities.[9] Previously, these instabilities were observed in both experimental[10–14] and numerical[15–20] studies, encompassing phenomena such as chaotic instability, low-frequency waxing and waning instability, transient mode switching, and longitudinal pulsed detonation instability. Among these instabilities, the high-frequency instability arises as a consequence of the oscillatory behavior exhibited by the height of the DW, and the occurrence of low-frequency instability can be attributed to the disparity between the measurement location and the actual location of the DW.[16]

Specifically, burnt gas bumps emerge, and the fuel refill zone becomes irregular when the inflow total pressure is decreased,[17,18] which consequently results in the periodic oscillation of the DW in terms of height. Zhang *et al.*[15] showed that the oscillation of the DW stems from the synergistic interaction between the fuel injection and transverse shocks following the DW. This dynamic interaction among the DW, the morphology of the fuel refill zone, and the rate of mass flow mutually impacts one another.[15] Later, the effects of the inflow total pressure and equivalence ratio were studied by Wang *et al.*[18,19] Their results indicated that the oscillation of the DW height emerged as the inflow total pressure (or mass flow rate) was decreased, and the equivalence ratio had a minimal effect on the stability of the rotating detonation waves (RDWs). More recently, the effect of wave multiplicity on the stability of RDWs was studied by Sheng *et al.*[20] Their investigation indicated that as the DW number increased, the oscillation of the DW height was noticeably suppressed. However, this stabilization of the detonation mainly resulted from the decrease in the DW height. For the stable operation of an RDE, a significant reduction in the DW height was considered undesirable because the DW height should not fall below a critical threshold value of approximately $h^* = (12 \pm 5)\ \lambda$ to ensure stable propagation; here, λ represents the size of the detonation cell.[16,21]

In conjunction with various influencing factors, these instabilities contribute to the formation of highly intricate flow field structures within the combustor of an RDE.[9,22] Notably, these structures include complex shock wave systems that exert a significant impact on the propagations of DWs, reactant injection processes, and other fluid-chemical dynamic behaviors within the combustor.[20] In practical applications, intensive oscillation of the RDWs may lead to perturbations of the flow field or even quenching of the flame front, which further deteriorates the smooth performance of RDEs. The influencing factors,[16,18] evolution characteristics,[11] and formation mechanisms[15] of the instability of RDWs were extensively investigated in the aforementioned studies. However, this problematic issue needs to be addressed and the effective enhancement of the stability of RDWs through an active avenue remains unsolved.

Another aspect of RDE that has gained significant attention in recent years is the combustion mode. Although RDEs are nominally detonation engines, both detonation and deflagration exist within the combustor.[17,23] Most of the fuel injected into an RDE is consumed by detonative combustion at the DW, whereas the remaining fuel is mainly consumed by deflagrative combustion on the deflagration surface.[17,23–25] Previous investigations showed that the existence of deflagration produced to parasitic combustion,[9] which could lower the performance of the RDEs. The combustion modes of the gaseous[23] and two-phase RDEs[24–26] have been thoroughly investigated, but comprehensive investigations of the time-evolution characteristics of both detonative and deflagrative combustion are lacking. Additionally, the impact of the inflow conditions on the combustion mode needs further study for a better understanding of the combustion characteristics in the RDEs.

Based on the above two issues, the objective of our study is to enhance the stability of the RDWs and consequently alleviate the performance output fluctuations. A novel swirling inflow strategy is proposed, and a series of two-dimensional numerical simulations of hydrogen-air-fueled rotating detonations are carried out to investigate the effects of the swirling inflow on the stability and combustion mode of rotating detonations. The remainder of this paper is organized as follows: The computational methods and their numerical implementations are introduced in Sec. II. The numerical results and analyses of the general features of the detonation flow field, the variations in the RDW, and the combustion mode under different inflow conditions are presented in Sec. III. Finally, conclusions are drawn in Sec. IV.

II. NUMERICAL METHODOLOGY AND IMPLEMENTATION

A. Governing equations and numerical methods

The flow field of a gaseous rotating detonation is essentially one kind of multispecies compressible reactive flow, which can be governed by the Navier–Stokes equations in combination with the species transport equations shown below:

$$\frac{\partial \rho}{\partial t} + \nabla \cdot (\rho \boldsymbol{U}) = 0, \tag{1}$$

$$\frac{\partial (\rho \boldsymbol{U})}{\partial t} + \nabla \cdot (\rho \boldsymbol{U}\boldsymbol{U}) + \nabla p - \nabla \cdot \bar{\bar{\tau}} = 0, \tag{2}$$

$$\frac{\partial (\rho E)}{\partial t} + \nabla \cdot \left(\rho \boldsymbol{U}\left(E + \frac{p}{\rho}\right)\right) = \nabla \cdot \left(-\boldsymbol{q} - \sum_i h_i \boldsymbol{J}_i + \bar{\bar{\tau}} \cdot \boldsymbol{U}\right) + \dot{\omega}_T, \tag{3}$$

$$\frac{\partial (\rho Y_i)}{\partial t} + \nabla \cdot (\rho \boldsymbol{U} Y_i) + \nabla \cdot \boldsymbol{J}_i = \dot{\omega}_i, \quad (i = 1, \ldots, N-1), \tag{4}$$

where ρ, p, T, and $\boldsymbol{U}$ denote the density, pressure, temperature, and velocity vector of the mixture, respectively, and t is the time. E represents the total energy per unit mass of the mixture and is expressed as $E = h - \frac{p}{\rho} + \frac{|\boldsymbol{U}|^2}{2}$, where h is the enthalpy of the mixture: $h = \sum_i Y_i h_i$. Here, $h_i = \int_{298.15\,K}^{T} C_{p,i} dT$; $h_i \mathit{and}\ Y_i$ are the sensible enthalpy and mass fraction of the ith species, respectively. In Eq. (4), N denotes the total number of species.

In the momentum equation [Eq. (2)], the stress tensor is calculated by $\bar{\bar{\tau}} = \mu\left[(\nabla \boldsymbol{U} + \nabla \boldsymbol{U}^T) - \frac{2}{3}\nabla \cdot \boldsymbol{U}\boldsymbol{I}\right]$, where $\boldsymbol{I}$ is the unity tensor. μ denotes the dynamic viscosity evaluated from Sutherland's law: $\mu = \frac{C_1 T^{3/2}}{T + C_2}$, with the two constants given by $C_1 = 1.672\,12 \times 10^{-6}\ \mathrm{kg/m\,s\,K^{1/2}}$ and $C_2 = 170.672\ \mathrm{K}$. In Eqs. (3) and (4), $\boldsymbol{q}$ is the flux vector of heat conduction computed by Fourier's law: $\boldsymbol{q} = -k\nabla T$. $\boldsymbol{J}_i = -\rho D_{i,m} \nabla Y_i$ and is the diffusive flux vector of the ith species, where $D_{i,m}$ denotes the mass diffusion coefficient for the ith species in the mixture and is obtained under an assumption of unity Lewis number: $D_{i,m} = \frac{k}{\rho C_p}$. Here, k is the thermal conductivity, and C_p is the specific heat of the mixture at constant pressure, which is given by $C_p = \sum_i Y_i C_{p,i}$. The specific heat of each species $C_{p,i}$ is modeled as a function of temperature using a NASA piecewise polynomial.[27]

The first three terms on the right-hand side of the energy equation [Eq. (3)] denote the energy transfers due to heat conduction, species diffusion, and viscous dissipation, respectively. The fourth term $\dot{\omega}_T$ represents the heat production rate due to chemical reactions and is calculated as $\dot{\omega}_T = -\Sigma_i h_i^0 \dot{\omega}_i$, where h_i^0 is the enthalpy of formation of the ith species. $\dot{\omega}_i$ denotes the mass production rate of the ith species and is computed as a summation over all Arrhenius reactions,

$$\dot{\omega}_i = M_{w,i} \sum_{r=1}^{N_R} \hat{R}_{i,r}, \tag{5}$$

where $M_{w,i}$ is the molar weight of the ith species. N_R is the total number of reactions, and $\hat{R}_{i,r}$ denotes the production rate of the ith species in mole in the rth reaction, calculated as follows:

$$\hat{R}_{i,r} = \Gamma\left(\nu''_{i,r} - \nu'_{i,r}\right)\left(k_{f,r} \prod_{i=1}^{N} [C_i]^{\nu'_{i,r}} - k_{b,r} \prod_{i=1}^{N} [C_i]^{\nu''_{i,r}}\right). \tag{6}$$

In Eq. (6), Γ denotes the third-body effects on the reaction rate, $\nu'_{i,r}$ and $\nu'_{i,r}$ are the stoichiometric coefficients of the ith species in the reactants and products of reaction r, respectively, while $k_{f,r}$ and $k_{b,r}$ are the forward and backward rate coefficients of reaction r, respectively. C_i is the molar concentration of the ith species: $C_i = \frac{\rho Y_i}{M_{w,i}}$. Note that only $N-1$ species transport equations toned to be solved, as in Eq. (4), and the mass fraction of the last species can be implicitly computed with the constraint that all species mass fractions sum to unity. Finally, to close the conservation equation system, the equation of state for ideal gas is as follows: $p = \rho R_s T$, where R_s is the specific gas constant of the mixture: $R_s = R_u \sum_i \frac{Y_i}{M_{w,i}}$, where R_u is the universal gas constant.

The above conservation equations are then solved using a robust density-based solver with the implementation of a finite volume method (FVM) based on Cartesian grids. The advection upstream splitting method (AUSM+)[28–30] is known for its accurate capture of shocks and contact discontinuities and, hence, is implemented herein to compute the convective flux. The second-order upwind scheme is used for the discretization of the convection terms, while the diffusion terms are discretized by a second-order central-differencing scheme. A second-order implicit backward method is adopted for time-marching. Moreover, the time step is dynamically adjusted during simulations to ensure that the Courant number does not exceed 0.2, resulting in a time step on the order of 10^{-9}–10^{-8} s. The detailed analysis and discussions regarding verification of the numerical schemes can be found in Appendix A.

Since premixed detonation is an extreme combustion phenomenon that is predominated by flow convection and chemical kinetics, the effects of turbulence are limited; hence, no turbulence model is adopted in the present study. A similar treatment was adopted by Sheng *et al.*[20] and Zhao *et al.*,[17,23] whose results showed that the utilization of the Navier–Stokes equations in RDW simulations with or without a turbulence model did not yield noticeable discrepancies in the outcomes.[31]

For the chemical kinetics, a chemical reaction mechanism[32] for the hydrogen–air combustion consisting of seven species (H_2, H, O_2, O, OH, H_2O, N_2) and seven elementary reactions is adopted. The details of the chemical model are listed in Table I. This chemical model has been validated for detonation simulations[33] and widely used in many precedent detonation and combustion-related numerical studies.[32–35]

B. Physical model and numerical setups

Although the configuration of a practical RDE is in the form of a three-dimensional annular chamber, the radial dimension of the combustor slot is much smaller than the circumferential and axial dimensions. Two-dimensional numerical simulations of the flow field of an RDE have been demonstrated to be effective and sufficiently accurate in capturing the key flow structures and the relevant dynamic features and, hence, have been extensively employed in the literature.[23,24,36] The unrolled RDE is schematically shown in Fig. 1. The circumferential and axial dimensions of the combustor simulated in this paper are 0.15 and 0.05 m, respectively; these are identical to the scales used in previous numerical studies.[36–40]

TABLE I. The hydrogen–air reaction mechanism. Notes: the Arrhenius equation: $k_{f,r} = A_e T^b e^{-\frac{E_a}{RT}}$. Units are: moles, centimeters, seconds, Kelvins, and calories. The third-body coefficients are: (6) $H_2 = 2.5$, $H_2O = 12$, $O_2 = 1$; (7) $H_2 = 1$, $H_2O = 6.5$, $O_2 = 0.4$.

	Reaction	A_e	b	E_a
(1)	$H_2 + O_2 = OH + OH$	1.70×10^{13}	0.00	48 000.0
(2)	$H + O_2 = OH + O$	1.20×10^{17}	−0.91	16 800.0
(3)	$OH + H_2 = H + H_2O$	2.20×10^{13}	0.00	5 150.0
(4)	$O + H_2 = OH + H$	5.06×10^{04}	2.67	6 290.0
(5)	$OH + OH = O + H_2O$	6.30×10^{12}	0.00	1 090.0
(6)	$H + OH + M = H_2O + M$	2.21×10^{22}	−2.00	0.0
(7)	$H + H + M = H_2 + M$	7.30×10^{17}	−1.00	0.0

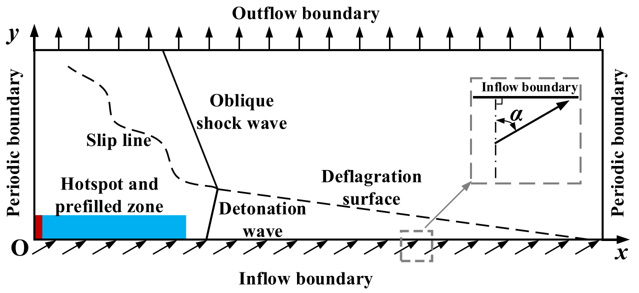

FIG. 1. Schematic diagram of the two-dimensional computational domain and boundary conditions of the RDE combustor. The hot spot and the prefilled zone are marked as the red and blue rectangles at the bottom-left corner, respectively.

To mimic the practical annular combustor and ensure that the RDWs can continuously propagate within the computational domain, the lateral boundaries are set as periodic boundary conditions, where flow information on corresponding nodes and edges is shared. At the inlet of the combustor, an inflow boundary condition is adopted, where a stoichiometric hydrogen–air mixture (also denoted as the "reactant" below) is injected through the inflow boundary with a fixed total pressure of $p_0 = 0.5$ MPa and total temperature of $T_0 = 300$ K. The isentropic expansion relation[41–43] of ideal gas is used to correlate the real-time inflow parameters such as static temperature and velocity imposed onto the inlet with the aforementioned total flow parameters based on the static pressure in the neighboring cells. In addition, the inflow boundary will be locally blocked if the interior chamber pressure is greater than the injection total pressure.[39,41,42] The direction of the inflow velocity vector with respect to the axial direction, as shown in Fig. 1, is defined as the swirling angle (denoted α), i.e., $\alpha = \arctan\left(\frac{u_{xi}}{u_{yi}}\right)$. A simple back-pressure outflow boundary condition[44,45] is set at the outlet, where all the flow variables are extrapolated from the internal flow field in the case of locally supersonic flow; however, a back pressure of $p_b = 1$ atm is enforced in the case of locally subsonic flow. In practical applications, swirling inflows may be implemented by adjusting the reactant injection angle or using an inlet guide vane.

The initial conditions of the flow field are depicted in Fig. 1, where a region near the inflow boundary ($0 < y < 8$ mm, $1 < x < 50$ mm) is prefilled with a quiescent stoichiometric hydrogen–air mixture with a static pressure of 0.1 MPa and a static temperature of 300 K, while the rest is filled with air at the same static pressure and temperature. To initiate an RDW, a hotspot ($0 < y < 8$ mm, $0 < x < 1$ mm) with a higher pressure of 3.5 MPa and a higher temperature of 2000 K is mapped at the bottom-left corner of the computational domain. Similar RDW initiation methods were also used in previous numerical studies, such as those by Luan *et al.*[46] and He *et al.*[47]

All simulated two-dimensional RDE cases are summarized in Table II. Apart from the baseline case, the coarsened case, and the refined case for grid independence tests, a total of six cases are used to

TABLE II. Information on the two-dimensional numerical cases.

Cases simulated	No.	Grid sizes, Δx (mm)	Grid sizes, Δy (mm)	Swirling angles, α (°)
Refined grids	A	0.1	0.05–0.2	0
Baseline grids	B	0.2	0.1–0.4	0
Coarsen grids	C	0.4	0.2–0.8	0
Negative swirling angles	1	0.2	0.1–0.4	−30
	2	0.2	0.1–0.4	−45
	3	0.2	0.1–0.4	−60
Positive swirling angles	4	0.2	0.1–0.4	+30
	5	0.2	0.1–0.4	+45
	6	0.2	0.1–0.4	+60

investigate the characteristics of the RDW flow fields under six different swirling angles ranging from $-60°$ to $+60°$. The grid resolution analyses of both the one-dimensional and two-dimensional detonation flow fields are presented in Appendices B and C, respectively. Notably, the effects of the swirling angle α, rather than the inflow velocity magnitude or the mass flow rate, on the stability of the DWs and the combustion mode are the focus of this study; hence, the inflow total pressure and total temperature are fixed in all cases (i.e., $p_0 = 0.5$ MPa and $T_0 = 300$ K) to eliminate the influences of the inflow velocity magnitude and/or the mass flow rate to produce more comparable results. The inflow velocity magnitude and consequently the mass flow rate may also have effects on the structures and characteristics of the RDW flow fields but are beyond the scope of the present study and will be further studied in the future.

III. RESULTS AND DISCUSSION

A. General features of rotating detonations with swirling inflow

Figure 2 shows the temperature contours of the flow fields with different swirling angles (i.e., case B and cases 1–6). All contours are captured during the stable propagation stage of the RDWs at approximately $t = 0.80$ ms. A single self-sustained RDW is successfully formed in the combustor in all simulated cases, and the basic structures of the flow field, including the DW, deflagration surface, oblique shock wave, and slip line as shown in Fig. 1, are all effectively captured. When the inflow is swirling (i.e., $\alpha \neq 0°$ as in cases 1–6), flow features in terms of the regularity of the fuel refill zone (i.e., the low-temperature regions in blue in Fig. 2), the smoothness of the deflagration surface and the homogeneity of reactant within the fuel refill zone significantly change in the RDW flow field as compared to those with a typical axial inflow (i.e., $\alpha = 0°$ as in case B).

The fuel refill zones exhibit the most noticeable alteration; in these zones, the shapes are significantly impacted by the swirling angle. For the baseline case [case B, $\alpha = 0°$, shown in Fig. 2(a)], the fuel refill zone becomes irregular due to the existence of the burnt gas bump. These burnt gas bumps have been extensively observed in previous numerical studies.[15,17–20,39] The formation of the burnt gas bumps is induced by localized injection stagnation points with a zero-inflow velocity at the inlet of the combustor, while the occurrence of the injection stagnation is attributed to the interaction between the transverse shock waves and the inlet.[15] As shown in Fig. 2, both positive and negative swirling angles could enhance the regularity of the fuel refill zone by suppressing the formation of the burnt-gas bumps.

The homogeneity of the reactant within the fuel refill zone, in terms of pressure distribution, for example, is the second feature that affects the RDW instability since the postdetonation state highly depends on the predetonation state. Figure 3 depicts the contours of the gradient magnitude of the hydrogen mass fraction of the RDW flow fields at different swirling angles of $\alpha = -60°$, 0°, and 60°. The profile of the fuel refill zone composed of the DW and the deflagration surface is clearly visible. In addition, the corresponding circumferential pressure distributions near the inlet ($y = 0.05$ mm) of the combustors and their locally enlarged views are shown in Figs. 4(a) and 4(b). The pressure pulses are spatially within the fuel refill zone with a nonswirling inflow [Fig. 4(b), $\alpha = 0°$]. Specifically, two pressure crests are observed within the fuel refill zone, with their circumferential locations aligning well with those of the burnt gas bumps, as marked by the gray dashed boxes in Figs. 3(b) and 4(b). This result is reasonable because both the pressure crests and the burnt gas bumps are related to the same factor, i.e., the injection stagnation at the inlet. This inhomogeneity of the predetonation pressure within the fuel refill zone had also been reported by Wu *et al.*[48] and considered as a key factor in the instability of RDWs. However, the implementation of a swirling inflow significantly suppresses the spatial pulses of pressure distribution in the fuel refill zone, regardless of whether the employed swirling angle is negative (e.g., $\alpha = -60°$ in Fig. 4) or positive (e.g., $\alpha = +60°$ in Fig. 4). No obvious pressure pulses in the fuel refill zones under these swirling inflows are observed, and the predetonation pressure decreases from the postdetonation value (due to Taylor rarefaction waves) more stably as compared to $\alpha = 0°$. The homogeneity of the reactant is improved by the swirling inflow, which is expected to be favorable to the stability of the RDWs.

Another swirling inflow-induced feature is the enhancement of Kelvin–Helmholtz (K–H) instability on the deflagration surface with large negative swirling angles (i.e., $\alpha = -45°$ and $-60°$). As clearly shown in Figs. 2(c) and 2(d), the deflagration surface becomes increasingly wrinkled as the negative swirling angle increases. To gain more insights into this phenomenon, distributions of the x-component of the velocity vector (u_x) at $y = 0.05$ mm near the inlet under different swirling angles are extracted and depicted in Fig. 5(a). Similar profiles of u_x are observed; specifically, the gas velocity drastically increases after the sweep of the RDW and then gradually decreases due to Taylor rarefactions following the leading DW. However, the averaged

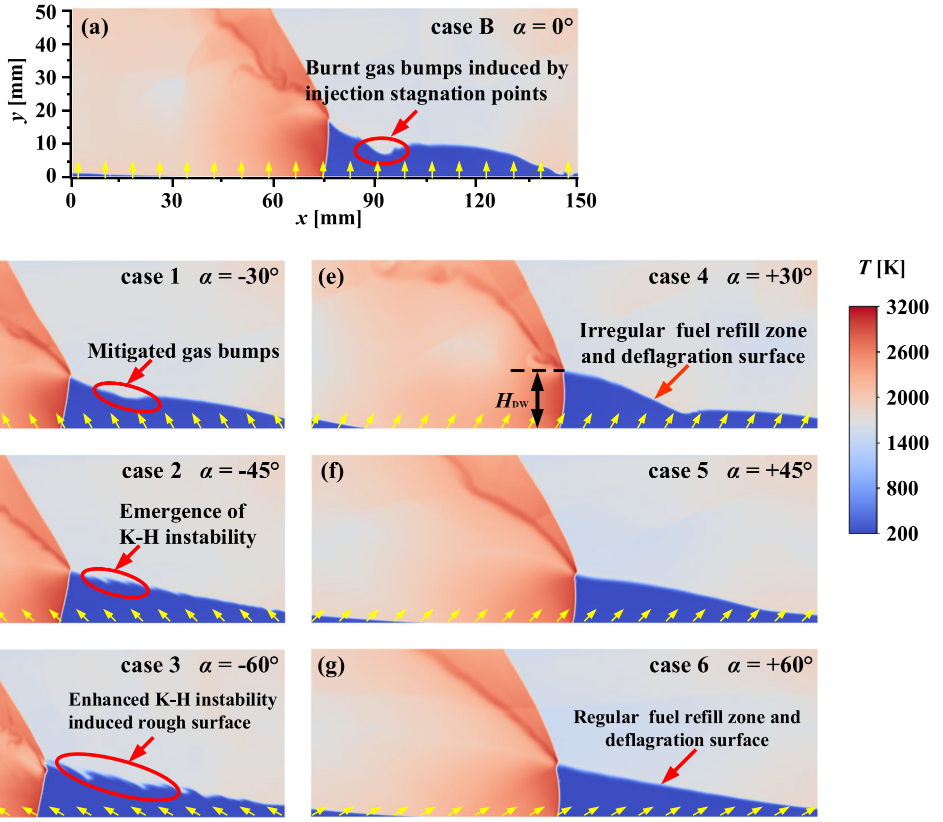

FIG. 2. Temperature contours under different swirling angles during the stable propagation stage of the RDW. The yellow arrows at the inflow boundary indicate the specific swirling angles.

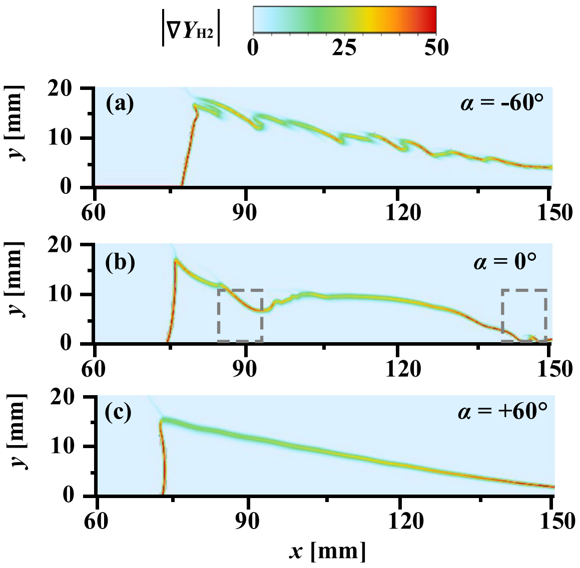

FIG. 3. Contours of the gradient magnitude of the hydrogen mass fraction. (a) Case 3, $\alpha = -60°$, (b) case B, $\alpha = -60°$, and (c) case 6, $\alpha = +60°$.

u_x [represented by the dashed line in Fig. 5(a)] is promoted by a positive α and impaired with a negative α. Figure 5(b) shows the profiles of the u_x gradient $\left(\left|\frac{\partial u_x}{\partial y}\right|\right)$ along an axial line approximately 5 mm ahead of the RDW under different swirling angles. A peak of the velocity gradient emerges near the deflagration surface, and the peak significantly increases with a large negative swirling angle (e.g., $\alpha = -60°$). This drastic increase in the spatial gradient of u_x produces the enhanced K–H instability, leading to the formation of a more wrinkled deflagration surface.

The oscillation of the height of the RDW [as marked as H_{DW} in Fig. 2(e)] is a key source of the RDW instability,[20,47,49] and its evolution is significantly influenced by the aforementioned features (i.e., the regularity of the fuel refill zone, the homogeneity of the reactant within the fuel refill zone, and the smoothness of the deflagration surface). At both positive and negative swirling angles, the regularity of the fuel refill zone and the homogeneity of the reactant inside the refill zone are improved, and these aspects are beneficial to the stability of the RDWs. However, K–H instability and consequently a wrinkled deflagration surface increase at large negative swirling angles. Therefore, the stability of the RDWs could be enhanced with a positive or a small negative swirling angle by improving the regularity of the fuel refill zone and the homogeneity of the reactant inside the refill zone without disturbing the smoothness of the deflagration surface.

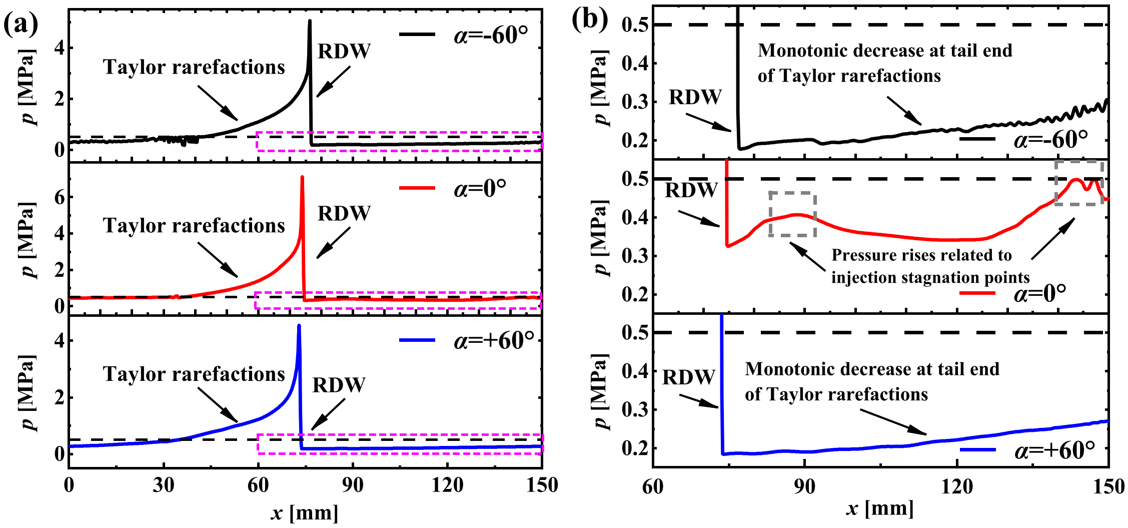

FIG. 4. Distributions of the (a) pressure near the inlet ($y = 0.05$ mm) under different swirling angle conditions and (b) the zoomed-in views. The scopes of the zoomed-in views are indicated by magenta dashed boxes in (a), and the black dashed horizontal lines represent the injection total pressure ($p_0 = 0.5$ MPa).

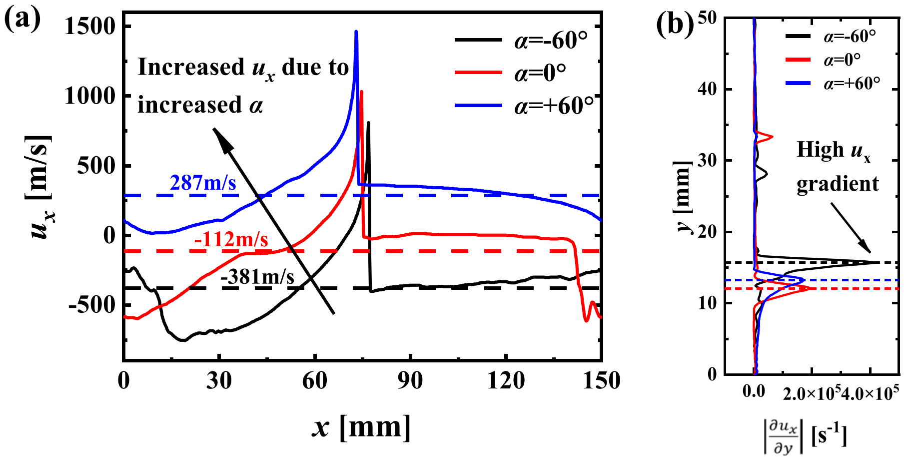

FIG. 5. (a) Distributions of u_x along a circumferential line near the inlet ($y = 0.05$ mm), and (b) profiles of $\left|\frac{\partial u_x}{\partial y}\right|$ along an axial line approximately 5 mm ahead of the RDW. The dashed horizontal lines in (a) indicate the spatially averaged u_x. The short-dashed lines in (b) refer to the location of the deflagration surfaces.

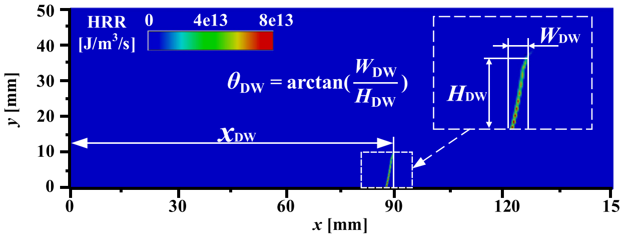

FIG. 6. Illustrations of x_{DW}, H_{DW}, W_{DW}, and θ_{DW}. The background contour is the distribution of the HRR for baseline case B at $t = 0.67$ ms.

B. RDW instability with swirling inflow

Periodic oscillation of the flame front will lead to instability of the flow field or even quenching of the RDWs in the combustor of an RDE: this deteriorates the performance of the engine in terms of both stability and reliability. Therefore, the effects of the swirling angle (α) on the stability of the RDWs will be discussed in this section in three aspects: the dynamics of the characteristic height (H_{DW}), the wave angle (θ_{DW}), and the wave speed (D) of the DW. Here, H_{DW} and θ_{DW} are defined and evaluated from the field of the heat release rate (HRR) of the instantaneous flow fields, as shown in Fig. 6. Specifically, H_{DW} is captured by tracking the maximum value of the y-coordinate of the region with an HRR greater than a critical value of 10^{13} J m^{-3} s^{-1}, and the characteristic width of the DW (W_{DW}) is estimated by the projection of the high-HRR region on the x-coordinate. Then, θ_{DW} can be approximated by $\theta_{DW} = \arctan\,(W_{DW}/H_{DW})$ since the DW does not always appear as a perfect straight line. In addition, the location of the DW (x_{DW}) can be captured and defined as the maximum x-coordinate of the high-HRR region ($>10^{13}$ J m^{-3} s^{-1}). Notably, the critical value of 10^{13} J m^{-3} s^{-1} for hydrogen–air detonations used in this study was first proposed by Zhao *et al.*[23] according to their numerical tests; this

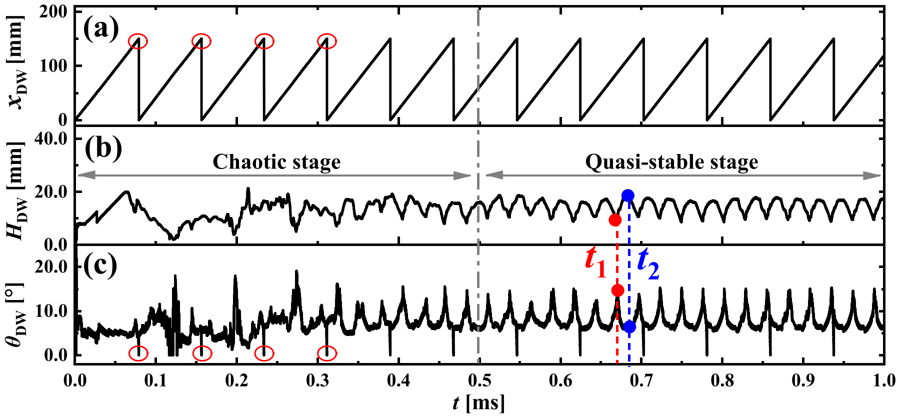

FIG. 7. Time histories of the (a) DW position, x_{DW}, (b) DW height, H_{DW}, and (c) DW angle, θ_{DW}, in baseline case B ($\alpha = 0°$). The critical instants when H_{DW} reaches its lowest and highest points are marked with vertical dashed lines colored in red and blue.

value was verified and then used to identify DWs in subsequent studies.[23–26] The effectiveness of this critical value will also be verified in Sec. III C of the present study.

The time histories of x_{DW}, H_{DW}, and θ_{DW} in baseline case B (i.e., $\alpha = 0°$) are plotted in Figs. 7(a)–7(c), respectively. As shown, the profile of x_{DW} is serrated with periodic sudden drops (marked by red circles) that are caused by the propagation of the RDW across the lateral periodic boundaries. Similar sudden drops (marked by red circles) are also visible in the profile of θ_{DW}. For a better demonstration of the figure and data, these nonphysics sudden drops in θ_{DW} are artificially masked in the figures of Sec. III B. A total of approximately 12 cycles of the RDW are observed within 1 ms. From Figs. 7(b) and 7(c), after a stage of chaotic fluctuation (approximately $t = 0$–0.5 ms), H_{DW} and θ_{DW} enter a quasi-stable stage with regular periodic oscillation.

In the quasi-stable stage, the waveforms of H_{DW} and θ_{DW} are similar in each cycle, both with three crests. To further elucidate the formation mechanism of the oscillations in H_{DW}, the contours of the temperature, normalized pressure gradient, and HRR at two critical instants when H_{DW} reaches its trough and crest (i.e., $t_1 = 0.67$ and $t_2 = 0.68$ ms in Fig. 7) are shown in Fig. 8. Evidently, at the critical instant of $t_1 = 0.67$ ms, the RDW sweeps right through a burnt gas bump where the fuel refill zone is narrowest [see Figs. 8(a)–8(c)], resulting in the lowest H_{DW}. When the physical time advances to the next critical instant [i.e., $t_2 = 0.68$ ms, see Figs. 8(e)–8(g)], the DW sweeps over the burnt gas bump marked in Fig. 8(a), and hence, the fuel refill zone becomes wider and a crest of the H_{DW} is reached. Additionally, θ_{DW} exhibits contrasting variations in comparison to H_{DW}, as is evident from Fig. 7; whenever H_{DW} reaches its crests (troughs), θ_{DW} always reaches its troughs (crests). This occurs because as the RDW sweeps through the burned gas bumps, it undergoes a clockwise rotation followed by a counterclockwise rotation.[19] The rotation of the DW finally leads to the oscillation of the θ_{DW}.[18,19] The oscillations of H_{DW} and θ_{DW} were also observed previously in both numerical[15,17,19,20] and experimental[10] studies.

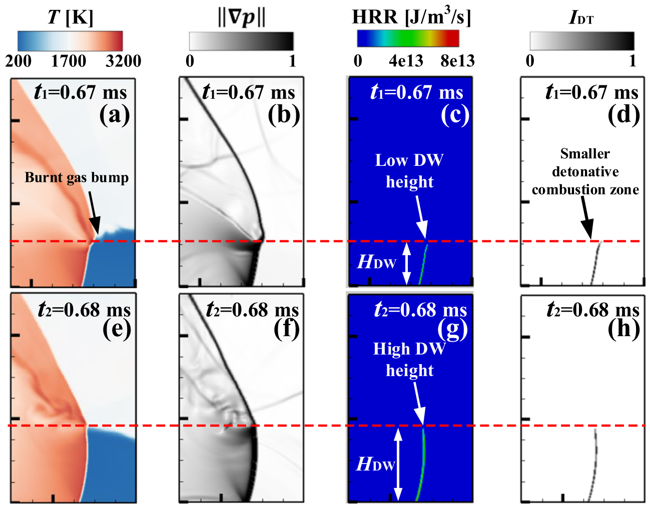

FIG. 8. Contours of the temperature, normalized pressure gradient ($||\nabla p||$), HRR and the detonation identifier (I_{DT}) at two critical instants in baseline case B ($\alpha = 0°$): (a)–(d) $t_1 = 0.67$ ms and (e)–(h) $t_2 = 0.68$ ms. The normalized pressure gradient is calculated as: $||\nabla p|| = 1 - \exp\left(\frac{-50|\nabla p|}{|\nabla p|_{max}}\right)$.

To clarify the effects of the swirling inflow, a comparison of the time evolutions of H_{DW} under negative and positive swirling angles are shown in Figs. 9(a) and 9(b), respectively. In addition, the time-averaged mean of H_{DW} and its standard deviation (STD) as functions of the swirling angle α are plotted in Fig. 10. Overall, the oscillation of H_{DW} is considerably dampened when either a negative or a positive swirling angle is implemented. For cases with positive swirling angles, the oscillation of H_{DW} estimated in terms of STD gradually decreases from 2.5 to 0.2 mm as the swirling angle α is increased from 0° to +60°. In the best case ($\alpha = +60°$), the H_{DW} STD is reduced by 92%, indicating excellent stabilization of the RDW. This occurs mainly because the burnt gas bumps gradually disappear as α increases from 0° to +60° (see Fig. 2). For cases with negative swirling angles, the oscillations are evidently dampened as well. The STD of H_{DW} is significantly decreased from 2.5 to 0.4 mm, with α ranging from 0° to −45°. The decrease in H_{DW} STD can also be attributed to the disappearance of burnt gas bumps (see Fig. 2). However, the situation in the case with $\alpha = -60°$ is abnormal. The H_{DW} STD increases when α is further increased from −45° to −60° (see the magenta box in Fig. 10) due to the enhanced K–H instability that leads to a wrinkled deflagration surface [see Figs. 2(d) and 3(a)]; this is also the reason that the black curve in Fig. 9(b) oscillates with a higher frequency. Moreover, the average H_{DW} for all cases remains almost unchanged when α ranges from

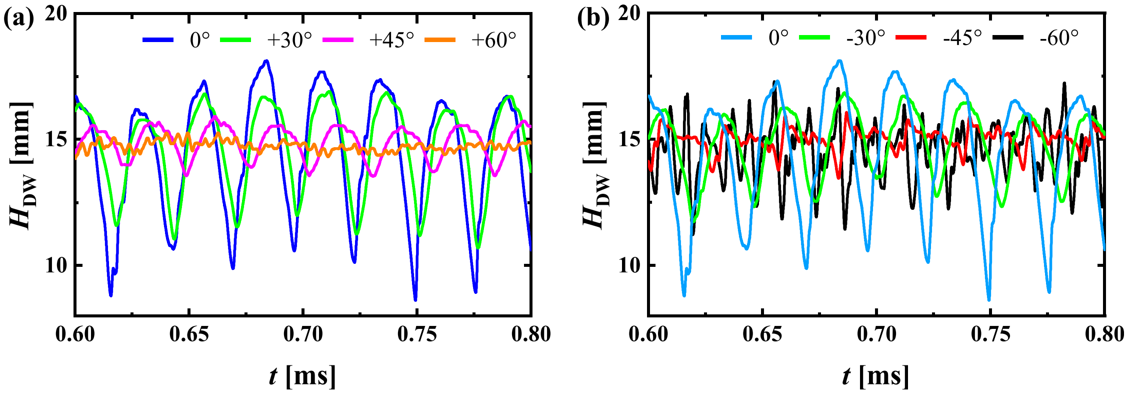

FIG. 9. Time histories of the H_{DW} under different inflow conditions with (a) positive and (b) negative swirling angles.

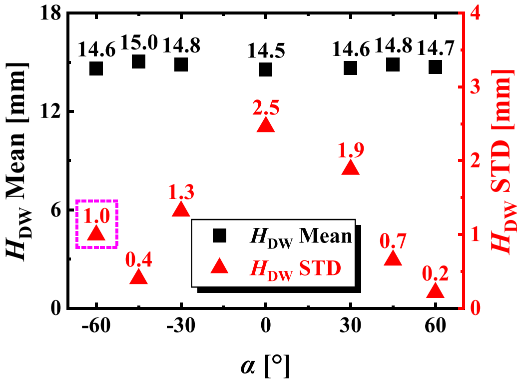

FIG. 10. Mean and STD of the H_{DW} as functions of α. The sampling is carried out within the stage of quasi-stable propagation of the RDW between 0.5 and 1.0 ms.

$-60°$ to $+60°$. Thus, the oscillation of the flame front is significantly reduced without compromising the averaged flame area, which is favorable for stable operation of the engine.

Figure 11 shows the time variations of the DW angle (θ_{DW}) under different swirling angles (α). All series of θ_{DW} experienced periodic oscillations after the initial chaotic stage. Qualitatively, the oscillation amplitude of θ_{DW} is significantly dampened when either a negative or positive swirling angle is imposed; this result is very similar to the variations in the amplitude of H_{DW}. Particularly, in the case where $\alpha = +60°$ [the orange curve in Fig. 11(a)], θ_{DW} remains almost constant after the initial chaotic stage, indicating an excellent stabilization effect of the swirling inflow. Moreover, the time-averaged mean and STD of θ_{DW} are summarized in Fig. 12. The STD of θ_{DW} is reduced by approximately 95% in the most optimized case ($\alpha = +60°$) compared to the baseline case ($\alpha = 0°$). The mean of θ_{DW} monotonically declined from 11.0° to 2.1° as the swirling angle α increased from $-45°$ to $+60°$. The cause of this trend could be a complicated interaction and coupling among the H_{DW}, the inhomogeneity of the fuel refill zone, and the injection stagnation points; this effect will need further investigation in future works. Moreover, both the mean and the STD of θ_{DW} show a reversed trend in the case of $\alpha = -60°$, which again is related to the enhanced K–H instability on the deflagration surface.

Figure 13 illustrates the evolution of the wave speed (D) of the RDW with reference to the combustor's framework under different swirling angles; this is calculated as the time derivative of the location of the RDW [i.e., x_{Dw} in Fig. 7(b)]. The critical moments when the RDW propagates across the periodic boundaries are excluded to avoid a nonphysics evaluation of D. Overall, the evolutions of D in the

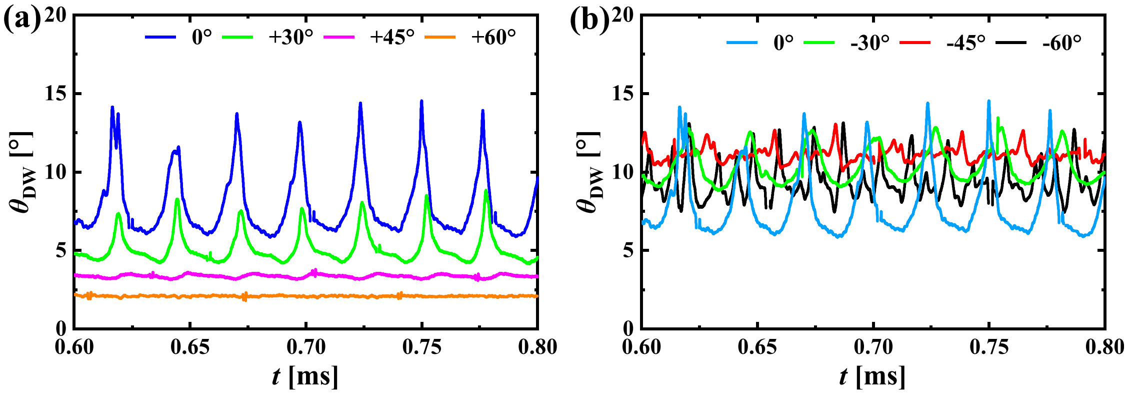

FIG. 11. Time histories of θ_{DW} under different inflow conditions with (a) positive and (b) negative swirling angles.

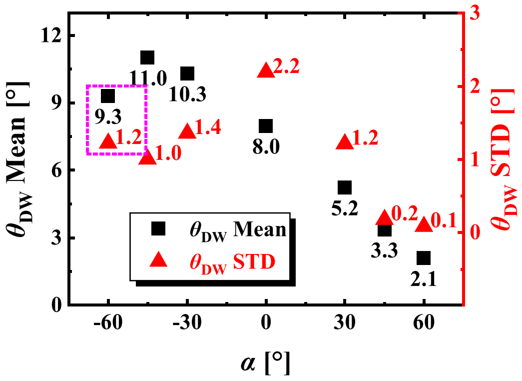

FIG. 12. Mean and STD of θ_{DW} as functions of α. The sampling is carried out within the stage of quasi-stable propagation of the RDW between 0.5 and 1.0 ms.

quasi-stable propagation stage undergo only small fluctuations (less than 8%) for all swirling angles. In terms of the time average, the D mean monotonically increases as the swirling angle α increases from $-60°$ to $+60°$. Specifically, D increases with a positive swirling angle and decreases with a negative swirling angle. This result could be attributed to the circumferential component of the inflow gas velocity (u_x) when a nonzero swirling angle is used. With a positive swirling angle, u_x is in the same direction as the propagation of the RDW, leading to an increase in the actual propagation speed of the RDW with reference to the RDE combustor, and vice versa. According to the classic Chapman–Jouguet (C–J) detonation theory,[50] the C–J pressure is highly dependent on the predetonation state, while the C–J detonation speed ($D_{C\text{-}J} = 1964.9$ m/s at $p = 0.1$ MPa and $T = 300$ K) with respect to the predetonation reactant is not sensitive to the predetonation pressure. Therefore, the RDW propagation speed can barely be controlled in the RDE combustor by the inflow total pressure when the traditional nonswirling axial inflow is imposed; this effect has been well demonstrated in previous studies.[17,18] As illustrated in Fig. 13(b), the RDW propagation speed D can be controlled in a considerably wide range from approximately 81%–114% of $D_{C\text{-}J}$ by adjusting the swirling angle. This result is promising since it provides a reliable way to control the propagation speed of the RDWs within the combustor.

C. Unsteadiness in the combustion mode and propulsion performance

Instability-induced fluctuations of the detonation front upstream (in the axial direction) of the RDE combustor consequently produces disturbances downstream, which could deteriorate the smooth performance of the engine. In Secs. III A and III B, a swirling inflow can significantly suppress the oscillations of the RDWs. In this section, the relevant effects of the swirling inflow on the combustion modes and the performance of the engine are discussed in detail.

1. The detonation identifier and instantaneous fuel consumption rates

Typically, the fuel injected into an RDE combustor is consumed in two distinct ways: the detonative combustion occurring behind the DW and the deflagrative combustion behind the deflagration surface.[9,17] Since detonative combustion is more favorable in terms of thermal efficiency than deflagrative combustion,[50] it is desirable in practical applications to consume more fuel by detonation rather than deflagration to achieve higher propulsion performance of the engine.

To identify the profiles of the detonative combustion regions, a detonation identifier for the hydrogen–air mixtures is defined based on the instantaneous HRR as follows:

$$I_{DT} = \begin{cases} 1, \ \log HRR \geq 13, \\ 0, \ \log HRR < 13. \end{cases} \tag{7}$$

Evidently, I_{DT} is a field variable, and its physical meaning is that in a region where detonative combustion occurs (characterized by $\mathrm{HRR} \geq 10^{13}\,\mathrm{J\,m^{-3}\,s^{-1}}$), $I_{DT} = 1$; otherwise, the nondetonative combustion (i.e., either deflagrative or noncombustion) regions are marked by $I_{DT} = 0$. As mentioned above, the critical value of $\mathrm{HRR} \geq 10^{13}\,\mathrm{J\,m^{-3}\,s^{-1}}$ for the hydrogen–air mixtures is based on the criterion first proposed by Zhao *et al.*,[23] and the reliability of using HRR to identify detonative combustion has been effectively validated in previous studies.[23–26] Zhao and Zhang[24] found that either doubling the critical value of HRR to $2\times10^{13}\,\mathrm{J\,m^{-3}\,s^{-1}}$ or halving it to $5\times10^{12}\,\mathrm{J\,m^{-3}\,s^{-1}}$ leads to a deviation of the results less than 5%. Some researchers also used this critical value of HRR ($10^{13}\,\mathrm{J\,m^{-3}\,s^{-1}}$) in

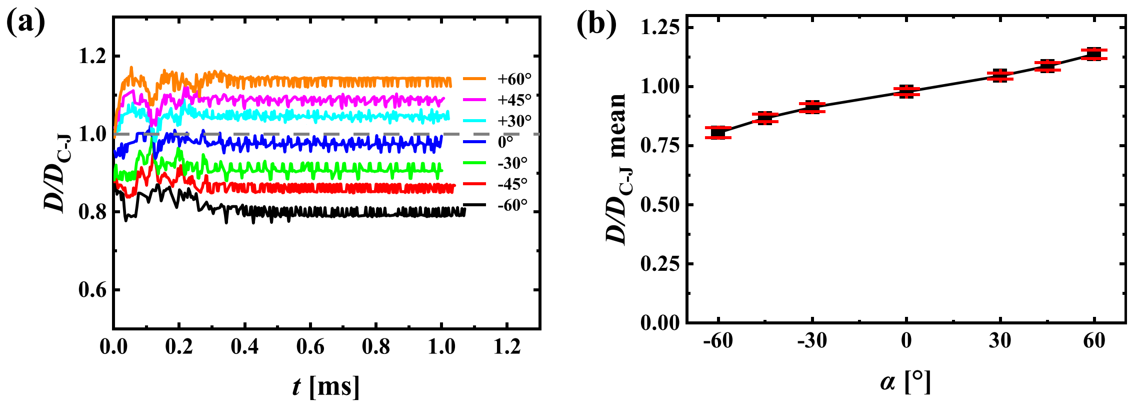

FIG. 13. Plots of the (a) time histories of $D/D_{C\text{-}J}$ under different swirling angles and the (b) mean of $D/D_{C\text{-}J}$ as a function of α.

calculating the detonation fraction of kerosene-fueled[51] and *n*-heptane-fueled[24] detonations. In Sec. III C 2, the reasonability and reliability of the present detonation identifier will be further discussed and demonstrated.

With the aid of I_{DT}, the instantaneous consumption rate of the injected fuel (represented by the consumption rate of hydrogen in this study) through detonative or deflagrative combustion (i.e., CR_{DT} or CR_{DF}, respectively) can be calculated by integrating the mass production rate of hydrogen $\dot{\omega}_{H2}$ over the entire computation domain V,

$$CR_{DT} = \int_V I_{DT} \cdot \dot{\omega}_{H2} dV, \tag{8}$$

$$CR_{DF} = \int_V (1 - I_{DT}) \cdot \dot{\omega}_{H2} dV. \tag{9}$$

Generally, both CR_{DT} and CR_{DF} are negative, indicating the consumption of hydrogen through a combustion process.

2. Combustion characteristics of an oscillating RDW

As discussed in Secs. III A and III B, the instability of RDWs manifests itself mainly in two aspects: (1) the oscillations of the H_{DW} and θ_{DW} due to the formation of the burnt gas bumps and the wrinkled deflagration surface, and (2) the oscillation of the predetonation state due to the inhomogeneity of reactant within the fuel refill zone. The joint effect of these two aspects of the RDW instability on the combustion modes along with the determination of the dominant effect will be analyzed and discussed in this subsection.

To quantitatively estimate the effects of the RDW instability on the combustion mode, Fig. 14 shows a comparison of the time histories of H_{DW}, CR_{DT}, and CR_{DF} in baseline case B ($\alpha = 0°$). The H_{DW}, CR_{DT}, and CR_{DF} oscillate periodically and synchronously with the same period; specifically, their oscillations simultaneously reach the crests or troughs. To gain more insights into this unsteady phenomenon, the contours of the HRR and I_{DT} at two critical instants when H_{DW}, CR_{DT}, and CR_{DF} reach their crests and troughs are selected for further analysis (i.e., $t_1 = 0.67$ and $t_2 = 0.68$ ms, as indicated by the red and blue vertical dashed lines in Fig. 14) and are already shown in Figs. 8(c) and 8(d) and Figs. 8(g) and 8(h), respectively. As shown in the figure, the profiles of the detonative combustion zone at these two instants closely resemble the corresponding intensive distributions of HRR. The locations of the detonative combustion zone identified by $I_{DT} = 1$ in Fig. 8 also align well with the locations of the DW indicated by intensive HRR. These results indicate that the detonative combustion zone can be effectively identified by I_{DT}.

According to the components (i.e., I_{DT} or 1 – I_{DT} and $\dot{\omega}_{\mathrm{H2}}$) of the integrands as shown in Eqs. (8) and (9), the periodical oscillations of CR_{DT} and CR_{DF} could be induced by the instability of the RDW in two ways. On the one hand, the profile of I_{DT} is highly dependent on the H_{DW}. Comparing Figs. 8(c) and 8(d) with Figs. 8(g) and 8(h), a higher H_{DW} always leads to a larger detonative combustion zone (characterized by $I_{\mathrm{DT}} = 1$). On the other hand, the variation in $\dot{\omega}_{\mathrm{H2}}$ can be caused by the inhomogeneity of the reactant within the fuel refill zone. Figure 15 shows the spatial distributions of density and temperature near the inlet at four instants of $t = 0.66$, $t_1 = 0.67$, $t_2 = 0.68$, and $t = 0.69$ ms in baseline case B ($\alpha = 0°$). The predetonation state (marked by the magenta circles in Fig. 15) of the right propagating RDW periodically oscillates in terms of both density and temperature. Specifically, at $t_1 = 0.67$ ms, the predetonation density and temperature are at their peaks, while at $t_2 = 0.68$ ms, the relevant density and temperature are at their troughs. Notably, the chemical reaction rate is very sensitive to temperature fluctuations, and it also changes with density. As a result, the $\dot{\omega}_{\mathrm{H2}}$ on the RDW periodically oscillates as the RDW propagates rightwards.

To quantitatively elucidate the effects of $\dot{\omega}_{\mathrm{H2}}$, Figs. 16(a) and 16(b) show the scatter plots of the temperature vs HRR at the two critical instants of $t_1 = 0.67$ and $t_2 = 0.68$ ms, respectively, of baseline case B ($\alpha = 0°$). These scatters are collected throughout all grid cells within the computational domain and colored by $\log|\dot{\omega}_{\mathrm{H2}}|$. There is a strong positive correlation between $\log|\dot{\omega}_{\mathrm{H2}}|$ and the HRR. Both the distribution structures and the regions characterized by $\log|\dot{\omega}_{\mathrm{H2}}| \geq 5$ or $\mathrm{HRR} \geq 10^{13}$ are nearly identical at both $t_1 = 0.67$ and $t_2 = 0.68$ ms. This correlation also re-illustrates the reasonability and reliability of using the HRR for detonation identification. Then, the scatter columns of $\dot{\omega}_{\mathrm{H2}}$ conditioned on $\log|\dot{\omega}_{\mathrm{H2}}| \geq 5$ at $t_1 = 0.67$ and $t_2 = 0.68$ ms are further plotted and compared in Fig. 17. Their average values are also calculated and represented by the horizontal dashed lines. The mean value of $\dot{\omega}_{\mathrm{H2}}$ (-3.33×10^5 kg/m^3/s) at $t_1 = 0.67$ ms is greater than that at $t_2 = 0.68$ ms (-2.79×10^5 kg/m^3/s). There also exists some scatters with extremely high $\dot{\omega}_{\mathrm{H2}}$ (marked by the gray rectangle in Fig. 17) at $t_1 = 0.67$ ms; these are attributed to the high density and temperature of the predetonation state.

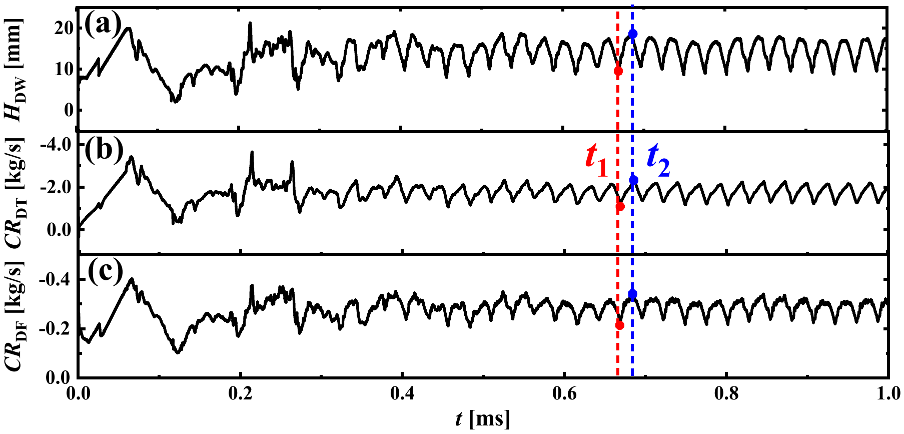

FIG. 14. Time histories of the (a) DW height H_{DW}, (b) detonative combustion rate CR_{DT}, and (c) deflagrative combustion rate CR_{DF}.

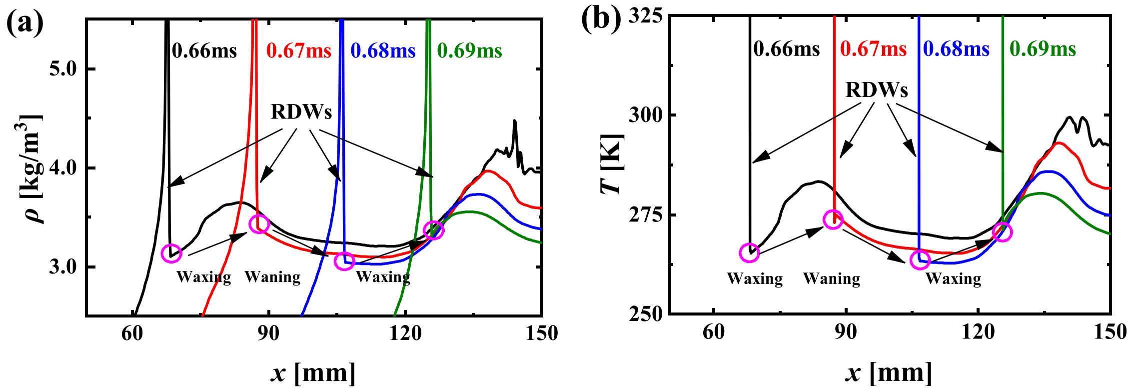

FIG. 15. Time evolutions of the spatial distributions of the (a) density and (b) temperature near the inlet in baseline case B ($\alpha = 0°$). The predetonation states of density and temperature are marked by magenta circles.

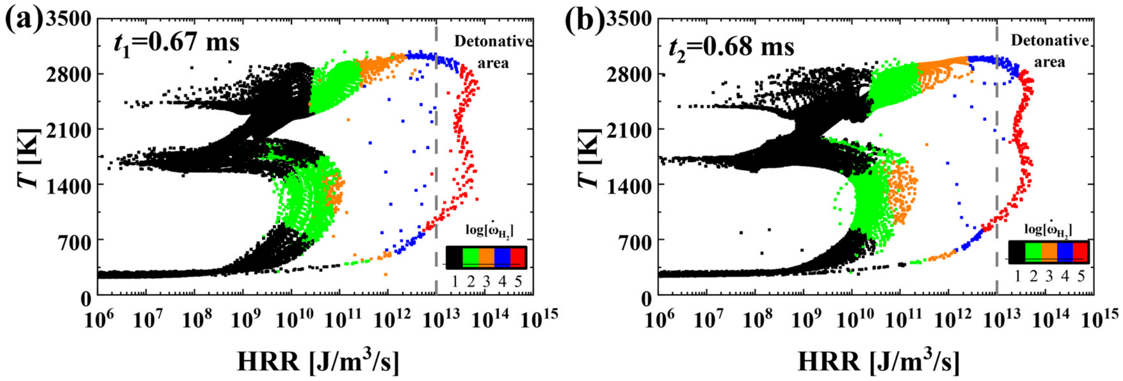

FIG. 16. Scatter plots of the instantaneous temperature vs HRR at (a) $t_1 = 0.67$ ms with the lowest RDW height and (b) $t_2 = 0.68$ ms with the highest RDW height in baseline case B ($\alpha = 0°$). The vertical gray dashed lines represent $\log \text{HRR} = 13$, whose right side indicates the detonative combustion region.

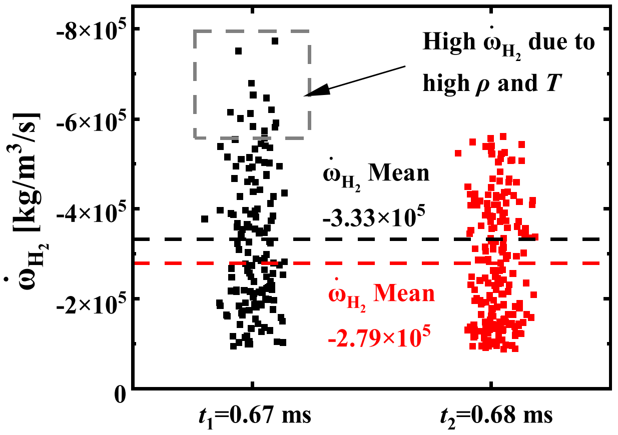

FIG. 17. Column scatter plots of the $\dot{\omega}_{H2}$ conditioned on $\log|\dot{\omega}_{H2}| \geq 5$ at $t = 0.67$ and $t = 0.68$ ms.

In summary, the mean $\dot{\omega}_{H2}$ at the lowest H_{DW} is higher than that at the highest H_{DW}, but CR_{DT} and CR_{DF} experience almost in-phase oscillations with that of H_{DW}. This deduction indicates that the oscillations of CR_{DT} and CR_{DF} are dominated by the oscillations of the area of the detonative combustion region rather than $\dot{\omega}_{H2}$, and the former is caused by the oscillation of H_{DW}. A higher H_{DW} always results in higher CR_{DT} and CR_{DF}. Specifically, the oscillation of the H_{DW} rather than the inhomogeneity of the reactant within the fuel refill zone is the key factor of the RDW instability that induces combustion oscillation in the RDE combustor.

3. Combustion characteristics of RDWs with swirling inflows

Figures 18(a) and 18(b) depict the temporal evolutions of CR_{DT} and CR_{DF} with various swirling angles. By using a swirling inflow (positive or negative), the oscillations in CR_{DT} and CR_{DF} are significantly dampened, especially at large swirling angles. For example, when a

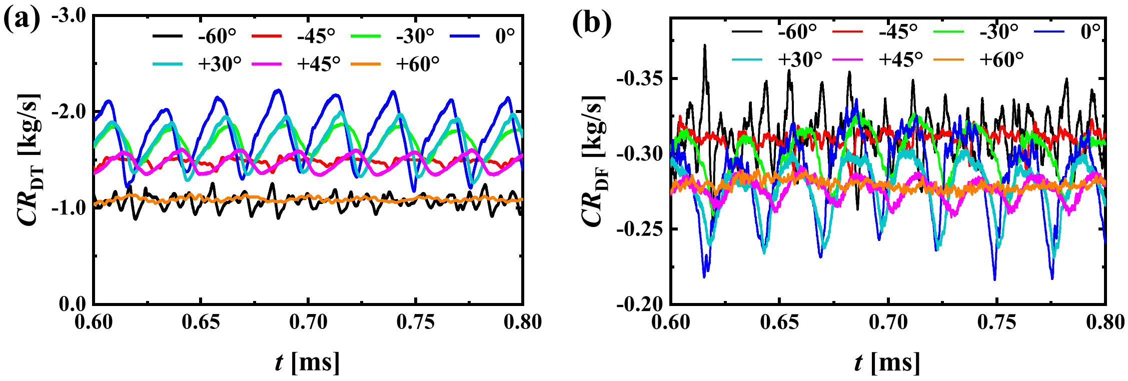

FIG. 18. Comparison of the time histories of (a) CR_{DT} and (b) CR_{DF} among different swirling angles.

swirling inflow with an angle of $\alpha = 60°$ is imposed (see the orange curves in Fig. 18), both CR_{DT} and CR_{DF} are nearly constant over time, indicating a remarkable reduction in their oscillatory behaviors and a highly stable combustion characteristic in the RDE combustor.

Quantitatively, Figs. 19(a) and 19(b) show the absolute values of the time averages with the STDs of CR_{DT} and CR_{DF}, respectively, during the quasi-stable propagation stage of the RDW from 0.5 to 1 ms. From Fig. 19(a), as the magnitude of the swirling angle increases in both the positive and negative directions, the $|CR_{DT}|$ mean exhibits a consistent decreasing tendency from 1.78 kg/s at $\alpha = 0°$ to approximately 1.07 kg/s at $\alpha = \pm 60°$. This phenomenon is caused by the inherent relationship between a larger swirling angle α and a reduced reactant mass flow rate (only the axial component of the inflow velocity vector contributes to the mass flow rate), which imposes limitations on the quantity of the reactants that can undergo combustion. The $|CR_{DF}|$ mean shows a slight increase when the swirling angle α increases in the negative direction from 0° to −60°. This increase can be attributed to the expansion of the deflagration surface area in the form of increasing wrinkles due to the K–H instability, as discussed in Sec. III A. As α increases in the positive direction from 0° to +60°, a slight decreasing tendency is observed in the $|CR_{DF}|$ mean (from 0.29 to 0.28 kg/s); this result is attributed to the reduction in the deflagration surface area due to the gradual diminishing of burnt gas bumps, as illustrated in Fig. 2.

The implementation of either a negative or positive swirling angle leads to the stabilization of the RDWs, resulting in remarkable reductions in the STDs of both CR_{DT} and CR_{DF}. As the magnitude of the swirling angle increases in both the positive and negative directions (except for $\alpha = -60°$), the STDs of both CR_{DT} and CR_{DF} significantly decrease. The decreasing percentages in the STD of the CR_{DT} reach approximately −93% at $\alpha = +60°$ and −89% at $\alpha = -45°$, while the decreasing percentages in the STD of the CR_{DF} are approximately −85% at $\alpha = +60°$ and −78% at $\alpha = -45°$. Similar to the observation for the H_{DW} in Fig. 10, an abnormal tendency is observed in the STDs of both CR_{DT} and CR_{DF} in Figs. 19(a) and 19(b) when the swirling angle changes from $\alpha = -45°$ to −60°. This result is self-explanatory since the oscillations in CR_{DT} and CR_{DF} are both dominated by the oscillation in the H_{DW}, as discussed in Sec. III C 2. Specifically, this abnormal tendency at $\alpha = -60°$ is also associated with the enhanced K–H instability due to a largely negative swirling inflow.

The efficiency of an RDE is at its highest level when the fuel is completely detonated rather than deflagrated; specifically, the detonation fraction (i.e., the percentage of detonative combustion) F_{DT} is an influential factor.[23] Here, F_{DT} is defined as the instantaneous

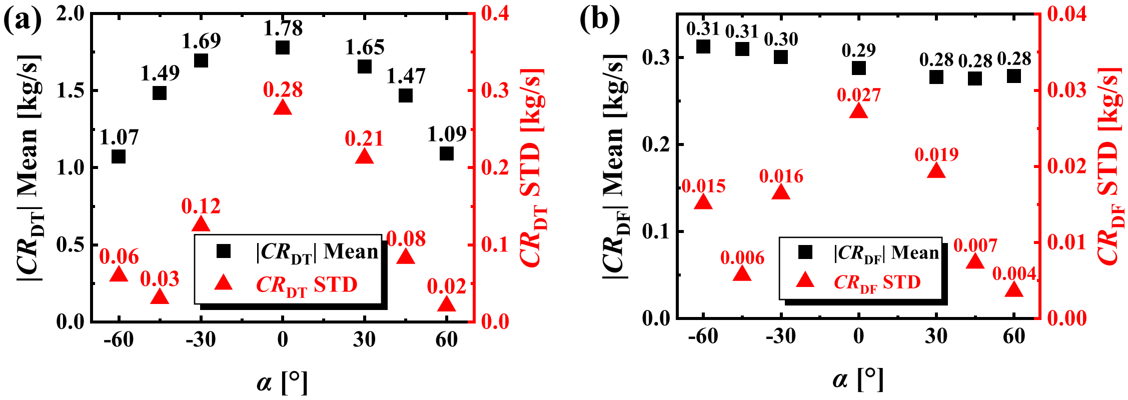

FIG. 19. Time-averaged values and STDs of (a) CR_{DT} and (b) CR_{DF} as functions of the swirling angle. The sampling interval is selected as 0.5–1 ms during the quasi-stable propagation stage of the RDW.

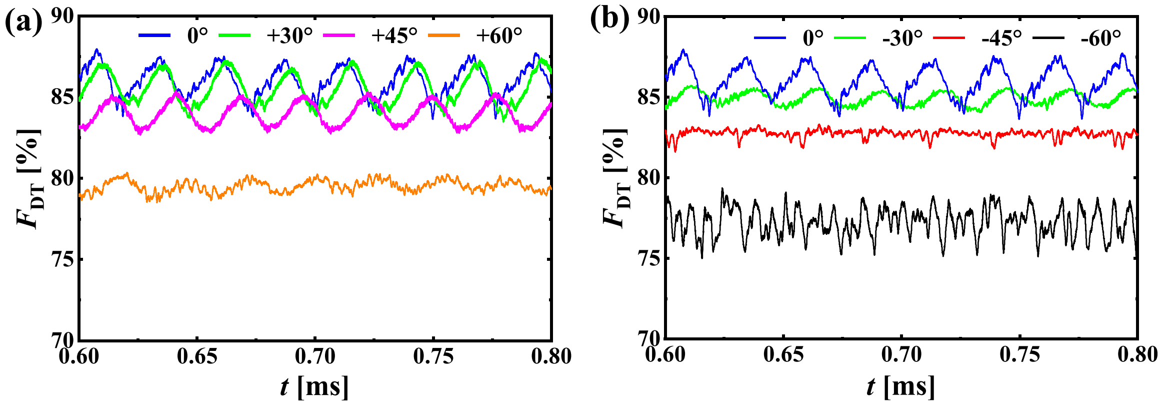

FIG. 20. Plots of the (a) time series of the detonation fraction (F_{DT}) with (a) positive and (b) negative swirling angles.

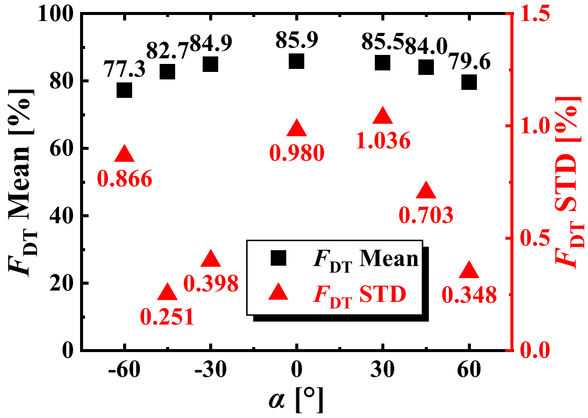

FIG. 21. Time-averaged mean and STD of the F_{DT}. The sampling interval is within the stage of quasi-stable propagation of the RDWs (0.5–1 ms).

percentage of detonative combustion occurring in the combustor and is calculated as follows:

$$F_{DT} = \frac{CR_{DT}}{CR_{DT} + CR_{DF}}. \tag{10}$$

Figures 20(a) and 20(b) show the variation of the F_{DT} as a function of time under different swirling angles during the quasi-stable propagation stage of the RDWs. Here, the oscillation pattern of the F_{DT} is greatly altered by the different swirling angles. Furthermore, the time-averaged means and STDs of the F_{DT} are summarized in Fig. 21 for quantitative analysis. On the one hand, the oscillation of the F_{DT} (i.e., the STD) is considerably reduced by the implementation of both increased negative and positive swirling angles, indicating more stable combustion modes. In the best case, the STD of the F_{DT} is reduced from 0.980% to 0.251%, with a reduction percentage of −77.39%, as the swirling angle changes from $\alpha = 0°$ to $-45°$. The increase in the F_{DT} STD at $\alpha = -60°$ is attributed to the high-frequency fluctuations in the H_{DW} caused by the enhanced K–H instability. On the other hand, the swirling inflow has an unfavorable effect for the F_{DT} mean; it is slightly decreased with the implementation of either negative or positive swirling angles. In the worst case, the time-averaged F_{DT} decreases from 85.9% at $\alpha = 0°$ to 77.3% at $\alpha = -60°$ with a moderate deterioration of 8.6%. This result indicates that the stabilized effects of the swirling inflows on RDWs potentially come at a cost of slightly deteriorated efficiency of the engine.

4. Propulsion performance with swirling inflows

Finally, to evaluate the propulsion performance of the RDE with different swirling inflows, the parameter of specific impulse I_{sp} is used:

$$I_{sp} = \int_{A_o} \frac{\left[\rho u_y{}^2 + (p - p_b)\right] dA_o}{g \dot{m}_R Y_{H_2}}, \tag{11}$$

$$\dot{m}_R = \int_{A_i} \rho u_y dA_i, \tag{12}$$

where A_O and A_i denote the outlet and inlet areas, respectively; u_y is the axial velocity; g is the gravity acceleration p_b is the backpressure (taken as 1 atm in this work); and Y_{H_2} denotes the mass fraction of hydrogen in the mixture. The fuel-based specific impulse is used here to make the results comparable to previous studies.[17,39,52] Figure 22 shows the variations in the I_{sp} as a function of time under different swirling angles during the quasi-stable propagation stage of the RDWs. Moreover, the corresponding time-averaged mean and STD of the I_{sp} are summarized in Fig. 23. For the baseline case with $\alpha = 0°$, the specific impulse I_{sp} is approximately 5500 s; this value is comparable to the results of previous studies.[17,39,52] When the swirling angle α changes from 0° to +60°, the oscillation of I_{sp} is significantly decreased (by −83.98% in terms of STD) with only a minimal loss in the mean of I_{sp} (−7.42%). The suppressed oscillation in I_{sp} can be attributed to the stabilized H_{DW} and F_{DT}. Nevertheless, in cases where a negative α is used, the situation becomes more complicated. With α ranging from 0° to −45°, the I_{sp} oscillation is gradually suppressed. However, as α is further increased from −45° to −60°, its oscillation becomes intensified (the I_{sp} SDT increases from 63.2 to 97.1 s). This abnormal increase again is due to the fluctuation of the H_{DW} caused by the distorted deflagration surface, which in turn is induced by enhanced K–H instability. In general, both negative and positive swirling angles can suppress the I_{sp} oscillation, and a greatly decreased I_{sp} oscillation indicates that the output smoothness of propulsion is substantially promoted by a swirling inflow.

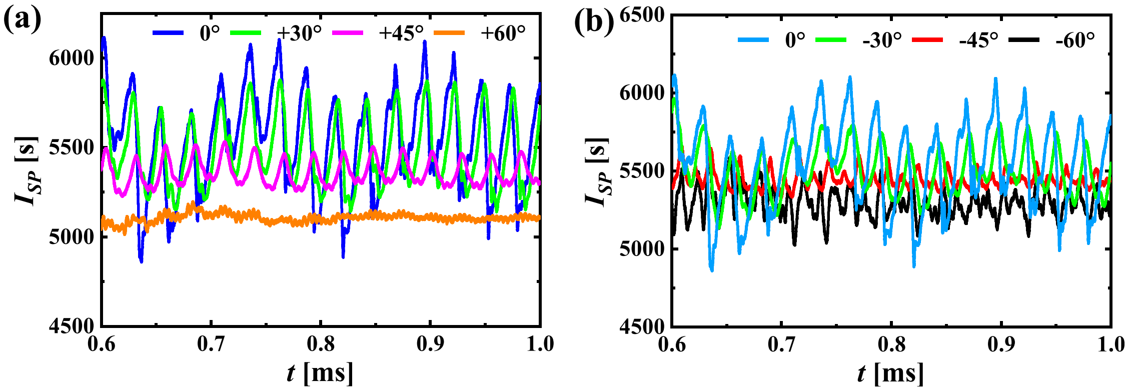

FIG. 22. Plots of the time series of the specific impulse I_{sp} under (a) positive and (b) negative swirling angles.

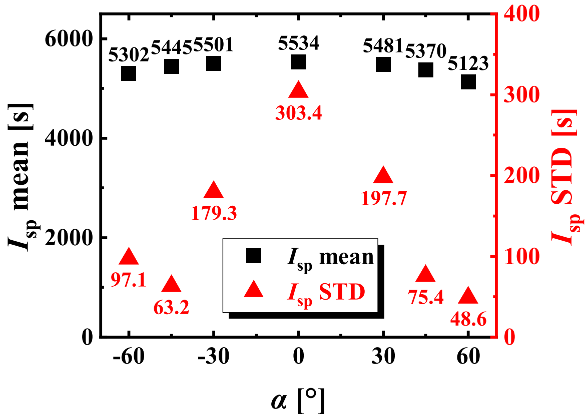

FIG. 23. Time-averaged specific impulse and its STD under different swirling angles. The sampling interval is within the stage of quasi-stable propagation of the RDWs (0.5–1 ms).

IV. CONCLUSION

In our study, a novel swirling inflow strategy is proposed to enhance the stability of the RDWs and the relevant combustion performance in the RDE combustors. A series of two-dimensional numerical simulations are carried out to validate the feasibility of this swirling inflow strategy. Specifically, the unsteady characteristics of the flow fields in the RDE combustor, including the instability of the RDW with respect to its height, inclined angle, and propagation speed and the combustion unsteadiness with respect to the instantaneous fuel consumption rates by detonation and deflagration and the detonation fraction, are systematically investigated; an emphasis is placed on the effects of the swirling angle.

The results show that the stability of the RDW is markedly enhanced using swirling inflows without a significant reduction in the time-averaged height of the RDW. Oscillations of the RDW in terms of both the height and the inclined angle are mitigated by increasing the swirling angle of the inflow in both the positive and negative directions through suppressing the formation of the burnt gas bumps and causing a more regular profile of the fuel refill zone. The inhomogeneity of the reactant within the fuel refill zone is also alleviated by the implementation of swirling inflow, indicating a more stable predetonation state. In addition, the propagation speed of the RDW can be controlled within a wide range from approximately 81%–114% of the C–J detonation speed by adjusting the swirling angle; this provides an alternative way to active wave speed control.

Moreover, a detonation identifier based on HRR is proposed to identify the instantaneous regions of detonative combustion and subsequently to evaluate the instantaneous fuel consumption rates of both the detonative and deflagrative combustion modes. The oscillations in these two instantaneous fuel consumption rates are both dominated by the periodic oscillation of the height of the detonation front rather than the inhomogeneity of the fuel refill zone. Therefore, the oscillations in these two combustion modes are improved by the swirling inflow. Nevertheless, the performance smoothness of the RDE in terms of specific impulses is significantly improved by the implementation of a swirling inflow at the cost of a small deficit (no more than 7.4%) in the time-averaged specific impulse. This deficit in the thrust performance can be attributed to the slight deterioration of the detonation fraction at both increased negative and positive swirling angles. Thus, a trade-off between the stability of the RDWs and the time-averaged thrust performance is potentially present.

ACKNOWLEDGMENTS

This work was supported by the National Natural Science Foundation of China (No. 12202374) and the opening project of the State Key Laboratory of Explosion Science and Technology (Beijing Institute of Technology, KFJJ23-20M).

AUTHOR DECLARATIONS

Conflict of Interest

The authors have no conflicts to disclose.

Author Contributions

Xinke Shao: Conceptualization (equal); Investigation (equal); Methodology (equal); Writing – original draft (equal). **Zijian Zhang:** Funding acquisition (equal); Resources (equal); Supervision (equal); Writing – review & editing (equal). **Lisong Shi:** Writing – review & editing (equal). **Hanli Huang:** Conceptualization (equal); Data curation (equal); Resources (equal). **Chih-Yung Wen:** Project administration (equal); Resources (equal); Supervision (equal); Writing – review & editing (equal).

DATA AVAILABILITY

The data that support the findings of this study are available from the corresponding author upon reasonable request.

APPENDIX A: VERIFICATION OF THE SOLVER AND NUMERICAL SCHEMES

To verify the solver and numerical schemes, numerical tests of the one-dimensional DW problem are carried out. The one-dimensional computational domain is initially prefilled with a stoichiometric hydrogen–air mixture at a pressure of 1 atm and a temperature of 300 K, and the DW is initiated by a hotspot with high pressure and temperature (3 MPa and 3500 K) at the left end of the domain ($0 < x < 2$ mm). The computational results are shown in Fig. 24. Our numerical methods effectively resolve the main features of the detonation flow field, including the self-sustained DW, the Taylor rarefaction waves, and the von Neumann spike. In addition, the length of the static burnt gas zone takes up approximately half of the total length, which aligns well with the analytic solution of one-dimensional detonation.[50]

Moreover, Table III summarizes the comparison between the numerical results and the theoretical C–J values in terms of temperature, pressure, and wave speed. Due to the propagation instability, the numerical results vary from instant to instant slightly. The relative errors are acceptable, albeit with a slightly larger discrepancy in C–J pressure when compared to those of temperature and wave speed. This might be caused by the weak instability in detonation propagation and the resulting pressure pulsation. In summary, the present solver is adequate for numerical simulation of detonations.

APPENDIX B: GRID RESOLUTION ANALYSIS I: ONE-DIMENSIONAL DW

Prior to conducting the two-dimensional numerical cases tabulated in Table II, three cases of the one-dimensional DWs with grid sizes of 0.1, 0.2, and 0.4 mm are used to estimate the discretization error and mesh sensitivity. The scale of the one-dimensional computational domain and initial conditions are the same as those in Appendix A. The results are summarized in Fig. 25. Figures 25(a) and 25(b) show that both the pressure and temperature distributions are almost independent of the given mesh resolutions. Figure 25(c) shows the time history of the DW speed; the DW speed also aligns well with each other and effectively agrees well the C–J theoretical values. In general, all three mesh resolutions effectively predicted the C–J pressure, temperature, and wave speed.

APPENDIX C: GRID RESOLUTION ANALYSIS II: TWO-DIMENSIONAL RDW

To further validate the grid independence, the time histories of H_{DW} (DW height) and CR_{DT} [instantaneous consumption rate of the injected hydrogen fuel through detonation, see Eq. (8)] obtained using different grid sizes are compared in Figs. 26(a) and 26(b). The grid information of the coarsened and refined cases can be found in Table II at Sec. II A. All three mesh resolutions effectively predicted

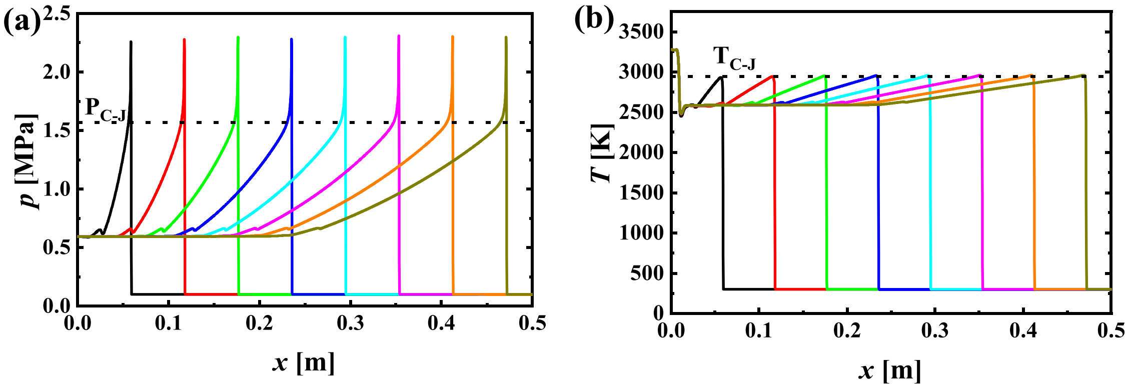

FIG. 24. Propagation process of the one-dimensional DW: (a) pressure distribution and (b) temperature distribution. Theoretical Chapman–Jouguet state values of pressure and temperature under identical predetonation conditions are indicated by horizontal black dotted lines.

TABLE III. Comparison of the one-dimensional computational results and the C–J theoretical values.

	$T_{C\text{–}J}$ (K)	$P_{C\text{–}J}$ (Bar)	D (m/s)
Numerical values	2930.17–2958.09	16.06–16.62	1950.09–1972.98
Theoretical predictions	2943.85	15.69	1964.90
Relative errors	−0.46% to 0.48%	2.36%–5.93%	−0.75% to 0.41%

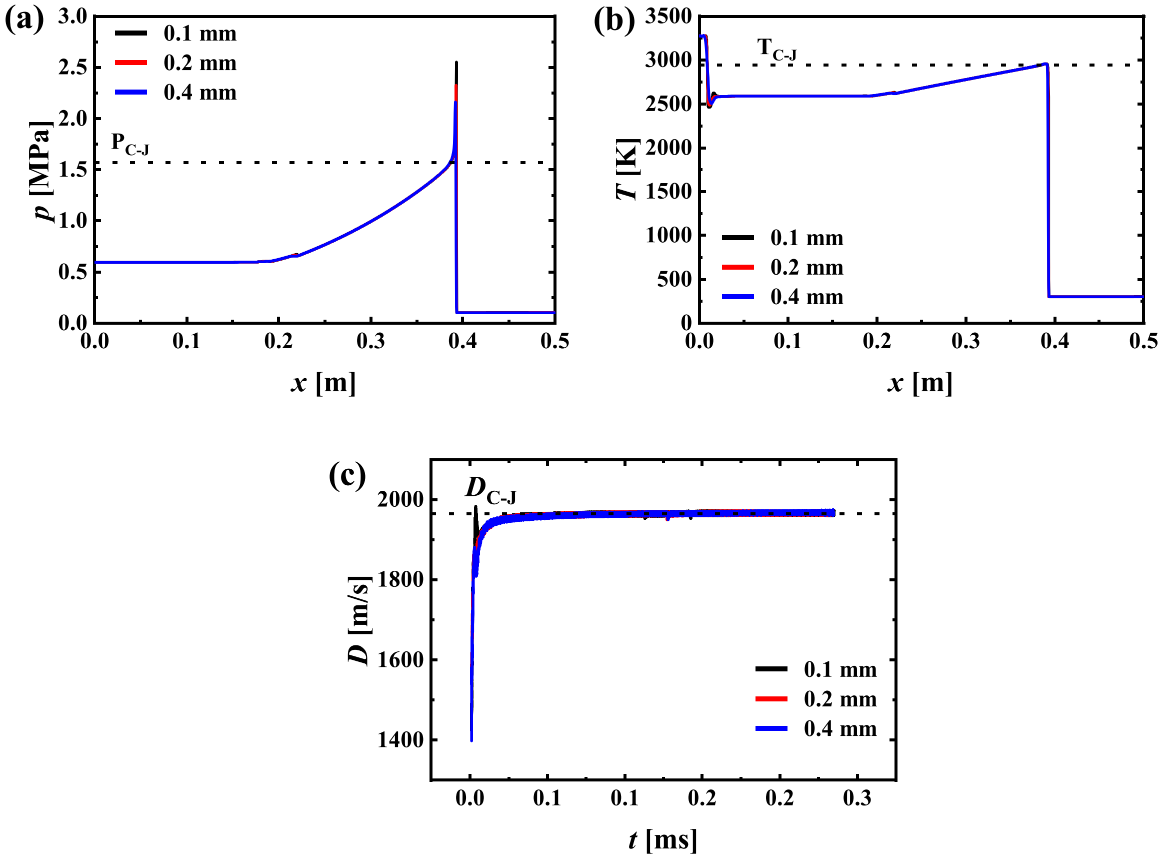

FIG. 25. Spatial distributions of (a) pressure and (b) temperature and (c) time evolution of the DW speed. Black dotted lines indicate the theoretical Chapman–Jouguet values under identical conditions.

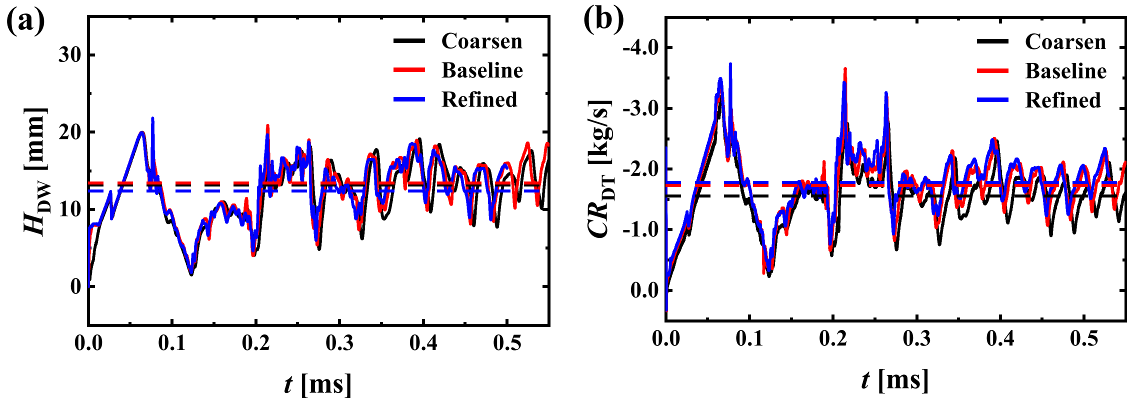

FIG. 26. Time series of (a) H_{DW} and (b) CR_{DT} in cases A, B, and C, respectively. The time-averaged values are marked with horizontal dashed lines.

the evolution patterns of both the instability of the RDW (characterized by H_{DW}) and the unsteadiness of the combustion mode (characterized by CR_{DT}). The time-averaged values in these three cases are marked with horizontal dashed lines. Evidently, the discrepancies in both time-averaged H_{DW} and CR_{DT} among the results attained using the baseline grids and the refined grids are minor and acceptable. Moreover, the time-averaged means of CR_{DT} and F_{DT} [detonation fraction, see Eq. (10)] are compared for

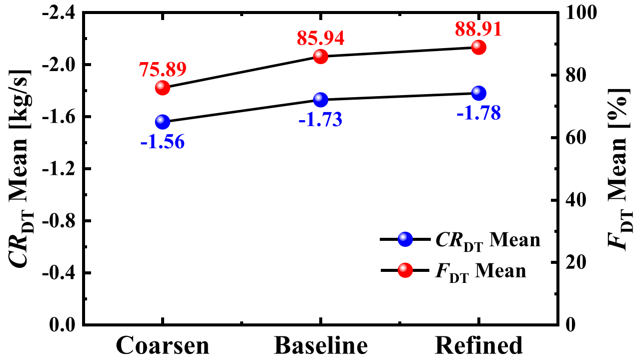

FIG. 27. Quantitative comparison of the time-averaged mean of CR_{DT} and F_{DT} under different grid resolutions.

quantitative comparison in Fig. 27. Considerable discrepancies are observed when the baseline mesh is coarsened. Nevertheless, only very minor discrepancies are observed when the baseline mesh is refined. Specifically, quadrupling the computational cost only leads to a discrepancy that is less than 3% in terms of both the time-averaged mean of the CR_{DT} and F_{DT}. This result indicates that the mesh resolution of the baseline grids used in the present study is adequate and maintains reasonable computational costs.

REFERENCES

[1] J. Koch and J. N. Kutz, "Modeling thermodynamic trends of rotating detonation engines," Phys. Fluids **32**(12), 126102 (2020).

[2] V. Anand and E. Gutmark, "Rotating detonation combustors and their similarities to rocket instabilities," Prog. Energy Combust. Sci. **73**, 182–234 (2019).

[3] Z. Zhang, C. Wen, W. Zhang, Y. Liu, and Z. Jiang, "Formation of stabilized oblique detonation waves in a combustor," Combust. Flame **223**, 423–436 (2021).

[4] Z. Zhang, C. Wen, C. Yuan, Y. Liu, G. Han, C. Wang, and Z. Jiang, "An experimental study of formation of stabilized oblique detonation waves in a combustor," Combust. Flame **237**, 111868 (2022).

[5] X. Han, Y. Liu, Z. Zhang, W. Zhang, C. Yuan, G. Han, and Z. Jiang, "Experimental demonstration of forced initiation of kerosene oblique detonation by an on-wedge trip in an ODE model," Combust. Flame **258**, 113102 (2023).

[6] L. Shi, E. Fan, H. Shen, C. Y. Wen, S. Shang, and H. Hu, "Numerical study of the effects of injection conditions on rotating detonation engine propulsive performance," Aerospace **10**(10), 879 (2023).

[7] X. K. Shao, Y. Kang, N. Li, X. L. Huang, J. S. Zhang, and C. S. Weng, "Mechanism and characteristics of thrust generated by a submerged detonation tube for underwater propulsion," Phys. Fluids **34**(10), 103321 (2022).

[8] P. Wolański, "Detonative propulsion," Proc. Combust. Inst. **34**(1), 125–158 (2013).

[9] V. Raman, S. Prakash, and M. Gamba, "Nonidealities in rotating detonation engines," Annu. Rev. Fluid Mech. **55**, 639–674 (2023).

[10] A. Naples, J. Hoke, J. Karnesky, and F. Schauer, "Flowfield characterization of a rotating detonation engine," AIAA Paper No. 2013-278, 2013.

[11] V. Anand, A. St George, R. Driscoll, and E. Gutmark, "Characterization of instabilities in a rotating detonation combustor," Int. J. Hydrogen Energy **40**(46), 16649–16659 (2015).

[12] Y. Liu, Y. Wang, Y. Li, Y. Li, and J. Wang, "Spectral analysis and self-adjusting mechanism for oscillation phenomenon in hydrogen-oxygen continuously rotating detonation engine," Chin. J. Aeronaut. **28**(3), 669–675 (2015).

[13] V. Anand, A. C. St. George, R. B. Driscoll, and E. J. Gutmark, "Statistical treatment of wave instability in rotating detonation combustors," AIAA Paper No. 2015–1103, 2015.

[14] C. Yang, X. Wu, H. Ma, L. Peng, and J. Gao, "Experimental research on initiation characteristics of a rotating detonation engine," Exp. Therm. Fluid Sci. **71**, 154–163 (2016).

[15] S. Zhang, S. Yao, M. Luan, L. Zhang, and J. Wang, "Effects of injection conditions on the stability of rotating detonation waves," Shock Waves **28**, 1079–1087 (2018).

[16] Y. Liu, W. Zhou, Y. Yang, Z. Liu, and J. Wang, "Numerical study on the instabilities in H_2-air rotating detonation engines," Phys. Fluids **30**(4), 046106 (2018).

[17] M. Zhao, J. M. Li, C. J. Teo, B. C. Khoo, and H. Zhang, "Effects of variable total pressures on instability and extinction of rotating detonation combustion," Flow. Turbul. Combust. **104**, 261–290 (2020).

[18] F. Wang, C. S. Weng, Y. W. Wu, Q. D. Bai, Q. Zheng, and H. Xu, "Effects of total pressures and equivalence ratios on kerosene/air rotating detonation engines using a paralleling CE/SE method," Defence Technol. **17**(6), 1805–1816 (2021).

[19] F. Wang and C. Weng, "Numerical research on two-phase kerosene/air rotating detonation engines," Acta Astronaut. **192**, 199–209 (2022).

[20] Z. Sheng, M. Cheng, and J. P. Wang, "Multi-wave effects on stability and performance in rotating detonation combustors," Phys. Fluids **35**(7), 076119 (2023).

[21] F. A. Bykovskii, S. A. Zhdan, and E. F. Vedernikov, "Continuous spin detonations," J. Propul. Power **22**(6), 1204–1216 (2006).

[22] G. Rong, M. Cheng, Z. Sheng, X. Liu, and J. Wang, "Investigation of counter-rotating shock wave phenomenon and instability mechanisms of rotating detonation engine with hollow combustor and Laval nozzle," Int. J. Hydrogen Energy **47**(54), 23019–23037 (2022).

[23] M. Zhao, M. J. Cleary, and H. Zhang, "Combustion mode and wave multiplicity in rotating detonative combustion with separate reactant injection," Combust. Flame **225**, 291–304 (2021).

[24] M. Zhao and H. Zhang, "Rotating detonative combustion in partially pre-vaporized dilute *n*-heptane sprays: Droplet size and equivalence ratio effects," Fuel **304**, 121481 (2021).

[25] Q. Meng, M. Zhao, H. Zheng, and H. Zhang, "Eulerian-Lagrangian modelling of rotating detonative combustion in partially pre-vaporized *n*-heptane sprays with hydrogen addition," Fuel **290**, 119808 (2021).

[26] Q. Meng, M. Zhao, Y. Xu, L. Zhang, and H. Zhang, "Structure and dynamics of spray detonation in *n*-heptane droplet/vapor/air mixtures," Combust. Flame **249**, 112603 (2023).

[27] B. J. McBride, "Coefficients for calculating thermodynamic and transport properties of individual species," Report No. NASA-TM-4513 (National Aeronautics and Space Administration, Office of Management, Scientific and Technical Information Program, 1993).

[28] M. S. Liou and C. J. Steffen, Jr., "A new flux splitting scheme," J. Comput. Phys. **107**(1), 23–39 (1993).

[29] M. S. Liou, "A sequel to AUSM: AUSM$^+$," J. Comput. Phys. **129**(2), 364–382 (1996).

[30] M. S. Liou, "A sequel to AUSM, Part II: AUSM$^+$-up for all speeds," J. Comput. Phys. **214**(1), 137–170 (2006).

[31] L. F. Zhang, J. Z. Ma, S. J. Zhang, M. Y. Luan, and J. P. Wang, "Three-dimensional numerical study on rotating detonation engines using reactive Navier-Stokes equations," Aerosp. Sci. Technol. **93**, 105271 (2019).

[32] R. A. Baurle, G. A. Alexopoulos, and H. A. Hassan, "Assumed joint probability density function approach for supersonic turbulent combustion," J. Propul. Power **10**(4), 473–484 (1994).

[33] M. Salvadori, P. Tudisco, D. Ranjan, and S. Menon, "Numerical investigation of mass flow rate effects on multiplicity of detonation waves within a H_2/Air rotating detonation combustor," Int. J. Hydrogen Energy **47**(6), 4155–4170 (2022).

[34] F. Génin, B. Fryxell, and S. Menon, "Simulation of detonation propagation in turbulent gas-solid reactive mixtures," AIAA Paper No. 2005-3967, 2005.

[35] M. Salvadori, I. B. Dunn, J. Sosa, S. Menon, and K. A. Ahmed, "Numerical investigation of shock-induced combustion of coal-H_2-air mixtures in a unwrapped non-premixed detonation channel," AIAA Paper No. 2020-2159, 2020.

[36] S. Jin, H. Zhang, N. Zhao, and H. Zheng, "Simulations of rotating detonation combustion with *in-situ* evaporating bi-disperse *n*-heptane sprays," Fuel **314**, 123087 (2022).

[37] W. Zhu and Y. Wang, "Effect of hydrogen flow rate and particle diameter on coal-hydrogen-air rotating detonation engines," Int. J. Hydrogen Energy **47**(2), 1328–1342 (2022).
[38] W. Zhu, Y. Wang, and J. Wang, "Flow field of a rotating detonation engine fueled by carbon," Phys. Fluids **34**(7), 073311 (2022).
[39] H. Chen, C. Si, Y. Wu, H. Hu, and Y. Zhu, "Numerical investigation of the effect of equivalence ratio on the propagation characteristics and performance of rotating detonation engine," Int. J. Hydrogen Energy **48**, 24074 (2023).
[40] Q. Meng, N. Zhao, and H. Zhang, "On the distributions of fuel droplets and in situ vapor in rotating detonation combustion with pre-vaporized *n*-heptane sprays," Phys. Fluids **33**(4), 043307 (2021).
[41] S. Yao and J. Wang, "Multiple ignitions and the stability of rotating detonation waves," Appl. Therm. Eng. **108**, 927–936 (2016).
[42] S. Yao, M. Liu, and J. Wang, "Numerical investigation of spontaneous formation of multiple detonation wave fronts in rotating detonation engine," Combust. Sci. Technol. **187**(12), 1867–1878 (2015).
[43] M. Hishida, T. Fujiwara, and P. Wolanski, "Fundamentals of rotating detonations," Shock Waves **19**, 1–10 (2009).
[44] L. Deng, H. Ma, C. Xu, X. Liu, and C. Zhou, "The feasibility of mode control in rotating detonation engine," Appl. Therm. Eng. **129**, 1538–1550 (2018).
[45] Q. Li, P. Liu, and H. Zhang, "Further investigations on the interface instability between fresh injections and burnt products in 2-D rotating detonation," Comput. Fluids **170**, 261–272 (2018).
[46] Z. Luan, Y. Huang, S. Gao, and Y. You, "Formation of multiple detonation waves in rotating detonation engines with inhomogeneous methane/oxygen mixtures under different equivalence ratios," Combust. Flame **241**, 112091 (2022).
[47] X. J. He, X. Y. Liu, and J. P. Wang, "Numerical study of the mechanisms of the longitudinal pulsed detonation in two-dimensional rotating detonation combustors," Phys. Fluids **35**(3), 036123 (2023).
[48] D. Wu, R. Zhou, M. Liu, and J. Wang, "Numerical investigation of the stability of rotating detonation engines," Combust. Sci. Technol. **186**(10–11), 1699–1715 (2014).
[49] F. K. Lu and E. M. Braun, "Rotating detonation wave propulsion: Experimental challenges, modeling, and engine concepts," J. Propul. Power **30**(5), 1125–1142 (2014).
[50] J. H. Lee, *The Detonation Phenomenon* (Cambridge University Press, 2008).
[51] F. Wang, C. Weng, and H. Zhang, "Semi-confined layered kerosene/air two-phase detonations bounded by nitrogen gas," Combust. Flame **258**, 113104 (2023).
[52] M. Zhao and H. Zhang, "Origin and chaotic propagation of multiple rotating detonation waves in hydrogen/air mixtures," Fuel **275**, 117986 (2020).